ICE SHEETS AND ICE VOLUME

Robert Thomas
Sigma Space, Gorzow Wlkp, Poland

Definition and introduction

An *ice sheet* is a large mass of ice resting on land that is continental or subcontinental in extent, with the ice thick enough to cover most of the underlying bedrock topography. Its shape is mainly determined by the dynamics of its gravity-driven outward flow. There are only two ice sheets in the modern world, in Greenland and Antarctica, but during glacial periods there were others. At the beginning of the *Cenozoic*, some 65 million years (Ma) ago, neither Greenland nor Antarctica supported an ice sheet. Then, as greenhouse gases in the atmosphere decreased, slow, irregular cooling allowed ice masses to accumulate and survive, first as mountain glaciers and then with the first continental ice sheet forming over Antarctica as early as 33 Ma ago. Further cooling led to extensive ice formation on Arctic land areas about 2.6 Ma ago, initiating the *Quaternary* series of ice ages with warmer interglacials at roughly 0.12 Ma intervals. Cycling between cold *glacial* and warmer *interglacial* periods is driven by periodic features of Earth's orbit, with ice sheets growing when sunshine shifts away from the Northern Hemisphere and melting when northern sunshine returns. These changes are amplified by feedbacks, such as greenhouse gas concentrations that rise and fall as the ice cover shrinks and grows, and greater reflection of sunshine caused by more extensive ice (Figure 1).

Human civilization developed during the most recent (*Holocene*) interglacial, extending over the past 11,000–12,000 years (ka). Holocene warming was interrupted during the Little Ice Age (about 1250–1850 AD), when the Greenland ice sheet and most Arctic glaciers reached their maximum Holocene extent. Since then, warming has resulted in Arctic-wide glacier recession, with similar responses becoming apparent more recently in Antarctica. These trends will continue if greenhouse gas concentrations continue to increase into the future (Table 1).

During the previous interglacial, 130–120 ka ago, Arctic summers were about 5 °C warmer than now and the Greenland ice sheet was considerably smaller than at present, with probable losses also from Antarctica, resulting in global sea level some 4–6 m above present values.

An ice sheet forms by the continual accumulation of snow on its surface. Over parts of an ice sheet, summers are warm enough to melt some of this snow, with some of the melt water percolating into the snow and refreezing and some running off the ice sheet into the ocean. The difference between local precipitation and melt-water runoff is the *surface mass balance*. As successive layers of snow build up, the layers beneath are gradually compressed into solid ice, at depths up to several tens of meters. The snow input is approximately balanced by glacial outflow, so the height of the ice sheet stays roughly constant through time. The difference between the mass of ice added by snowfall and that lost by runoff and ice motion is the *total mass balance*. The ice is driven downhill by gravity, from the highest points in the interior to the coast, where it melts at lower, warmer elevations or breaks off as icebergs. In contrast to Greenland, losses by surface melting are small in Antarctica and are primarily from the northern Antarctic Peninsula and the northernmost fringes of East Antarctica. The ice sheet spreads under its own weight, partly by *internal deformation* that increases with the cube of the driving stress which is proportional to the product of ice thickness and ice-surface slope. Internal deformation predominates where the ice is frozen to its bed and is typically slow. Where the bed of the ice sheet is at the melting point, ice may move more rapidly by

E.G. Njoku (ed.), *Encyclopedia of Remote Sensing*, DOI 10.1007/978-0-387-36699-9,

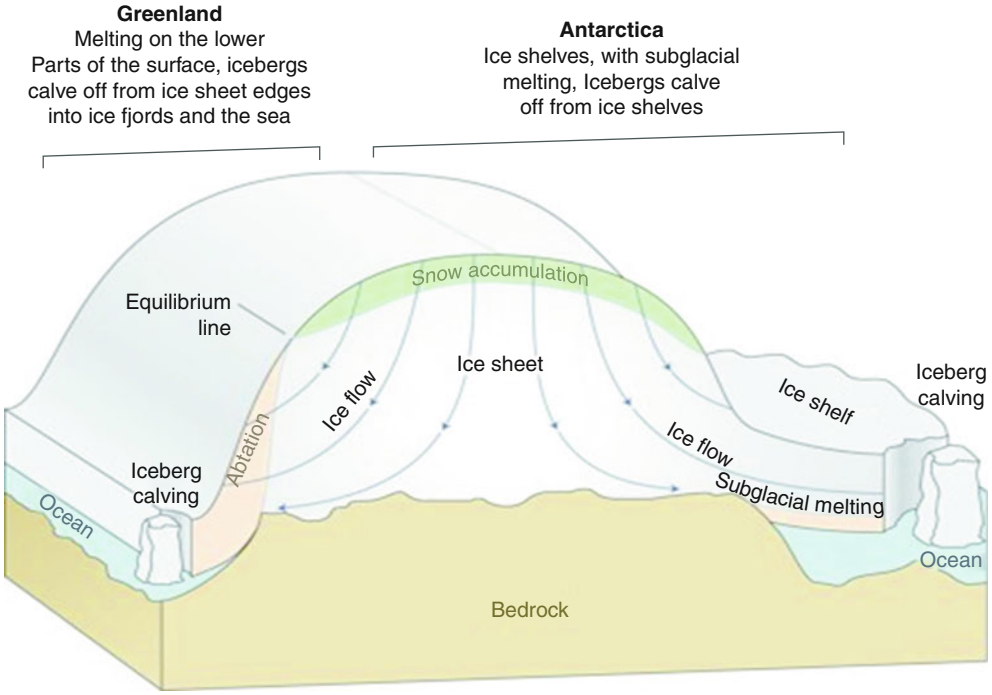

Ice Sheets and Ice Volume, Figure 1 Ice sheets showing the main features of those in Greenland (*left* of Figure) and Antarctica (*right*) (Source: K. Steffen, CIRES/University of Colorado).

Ice Sheets and Ice Volume, Table 1 The present areas and volumes of the two ice sheets, with estimates of the potential sea-level rise if they were to melt completely

	Area covered (million km^2)	Ice volume (million km^3)	Potential sea-level rise(m)
Ice sheets (total)	14.0	28	64
Greenland	1.7	3	7
Antarctica	12.3	25	57

sliding over its bed or by the deformation of water-saturated basal moraine and mud. This rapidly moving ice is generally channeled along bedrock troughs, which become further deepened as they are eroded by the moving ice. *Ice streams* are "jets" of faster ice flanked by slower flowing parts of an ice sheet, becoming outlet glaciers near the coast, where many are flanked by rock (Figure 2). Thus, for example, the fast-moving Jakobshavn Isbrae starts as an ice stream about 100 km inland that flows along a deep bedrock trough but is flanked by rock before calving *icebergs* into a long fjord on the west coast of Greenland.

The Antarctic ice sheet

Antarctica is the fifth largest and most southerly continent and is generally divided into two major regions: *West Antarctica*, including the *Antarctic Peninsula*, in the Western Hemisphere and *East Antarctica* in the Eastern Hemisphere. The *Transantarctic Mountains* separate the two, extending 3,000 km between the Atlantic and Pacific coasts. Most of Antarctica is covered by ice, with thick, grounded *inland ice* resting on a solid bed, and the floating *ice shelves* formed partly from ice flowing onto the ocean across the *grounding line* and partly from snow that falls onto them. The inland ice and the ice shelves together constitute the ice sheet, which is surrounded by ephemeral *sea ice*. Inland ice (ice shelf) ranges in thickness up to 5 km (1.5 km), with an average of about 2,400 m (600 m). Antarctica is, on average, by far the highest of the continents, with surface elevations rising to 4,000 m in central East Antarctica. The South Pole lies within the continent, which is completely surrounded by the ocean. The ice sheet was considerably larger during the Last Glacial Maximum, some 20,000 years ago, and retreated to near its present extent within the last several thousand years and perhaps is still retreating (Figure 3).

Separation of Southern Hemisphere continents from *Gondwanaland* finally left Antarctica isolated when *Drake's Passage* separated South America from the Antarctic Peninsula about 30 million years ago. This allowed uninterrupted circulation of the *Circumpolar Current* in the *Southern Ocean*. The combination of continuous oceanic and atmospheric circumpolar circulation around Antarctica led to cooling of the now isolated continent and formation of the ice sheet. Outflow from the inland ice is organized into a series of drainage basins, separated by

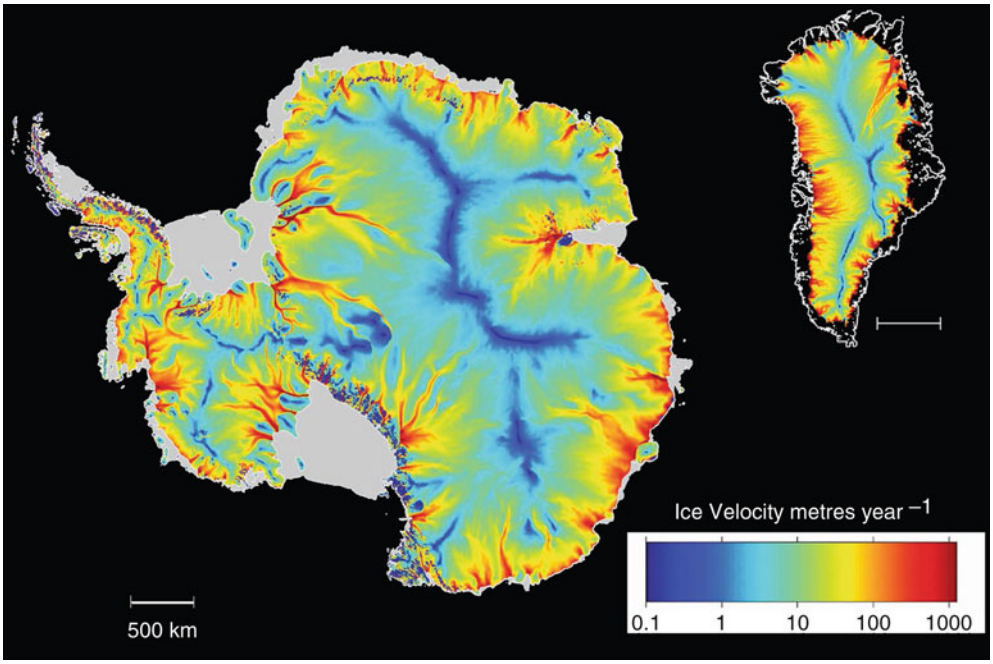

Ice Sheets and Ice Volume, Figure 2 Estimated "balance" ice velocities for the ice sheets in Antarctica (*left*) and Greenland (*right*). Note that the surface velocity scale is logarithmic. The *gray* areas around Antarctica are floating ice shelves. The *black* coastal areas around Greenland are ice-sheet-free mountains, which include some glaciers and ice caps. Ice discharge at these velocities exactly balances the mass added by snowfall (Allison et al., 2009, copyright Antarctic Science Ltd 2009).

Ice Sheets and Ice Volume, Figure 3 The Antarctic ice sheet and ice shelves. Some marginal seas are named, and Drake's Passage is to the north of the Antarctic Peninsula (Bentley et al., 2007).

ice divides, much like water flow on other continents. Most drainage basins concentrate the flow into either narrow outlet glaciers, particularly through the Transantarctic Mountains, or fast-moving ice streams, which are surrounded by slow moving ice rather than rock walls. Flow speeds increase toward the coast, because of increasing total upstream snowfall and because the ice generally thins to seaward. Where there is convergence into an outlet glacier or ice stream, the speed of flow is increased even more and can reach more than a kilometer per year.

The *West Antarctica ice sheet* (WAIS) flows mostly into the *Ross Ice Shelf* in the Ross Sea, the *Filchner/Ronne Ice Shelf* in the Weddell Sea, and smaller ice shelves in the *Amundsen Sea* which lies between the Bellingshausen and Ross Seas. The two big ice shelves are each about the area of Spain. Driven by gravity, ice shelves spread out over the ocean under their own weight, supplied with ice partly from tributary glaciers and ice streams, partly from snow that falls on their surfaces, and in some cases partly from ice frozen at basal interfaces with the ocean. Basal melting is far more common than freezing and can be as high as tens of meters per year and accounts for a large fraction of total losses, with iceberg calving from seaward ice fronts responsible for the rest. Where ice shelves run aground on shoaling seabed, *ice rumples* or *ice rises* are formed. Ice rumples are dragged along by surrounding ice shelf to move slowly over the sea bed; ice rises are stationary and dome shaped, with their own patterns of outward ice motion.

The Greenland ice sheet

The Greenland ice sheet occupies a latitude band extending from 60 to 80 N and covers an area of 1.7 million square km. With an average thickness of 1,600 m, it has a total volume of approximately 3 million cubic km – equivalent to a sea-level rise of about 7 m. It consists of a northern dome and a southern dome, with maximum surface elevations of approximately 3,200 m and 2,850 m, respectively, linked by a long saddle with elevations around 2,500 m. Bedrock beneath much of the ice sheet is close to sea level, but the ice sheet is fringed almost completely by coastal mountains through which the ice sheet is drained by many glaciers (Figure 4).

The ice sheet in Greenland differs substantially from that in Antarctica, which is almost ten times larger in volume. Antarctica straddles the South Pole and has a dominant influence on its own climate and on the surrounding ocean, with cold conditions even during the summer and around its northern margins. Away from the coast, much of Antarctica is a cold desert, with very low precipitation rates. There is little surface melting, even near the coast, and most of the melt water soaks into underlying snow and refreezes. Because of the cold conditions, vast floating ice shelves exist around much of the continent. Ice drainage is primarily by glaciers and ice streams, some of which penetrate deep into the heart of the ice sheet, moving at maximum speeds of a few

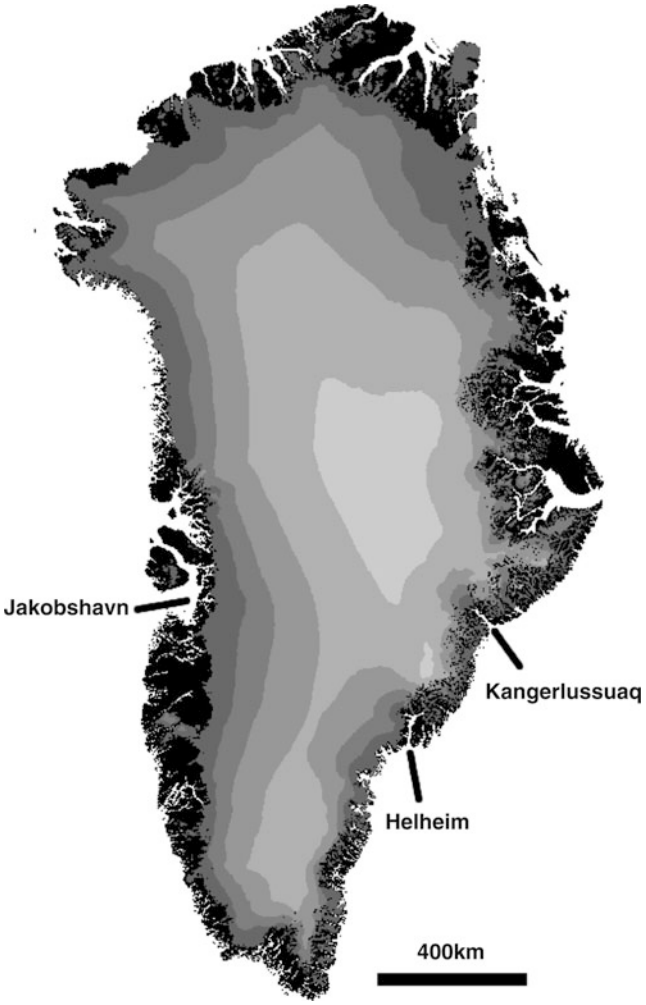

Ice Sheets and Ice Volume, Figure 4 The Greenland ice sheet, showing key glaciers. *Black* denotes rock, and *gray* denotes ice, shaded in 500 m elevation bands with the highest contour at 3,000 m (Prepared by S. Manizade).

hundred meters per year, apart from a few exceptions. Most glaciers and ice streams flow into ice shelves, which are also fed by snow accumulation on their surfaces. The ice shelves thin toward their seaward ice fronts, partly by ice creep and partly by basal melting, with melting rates generally of a few tens of centimeter/year, but increasing to tens of meters/year near the grounding lines of some ice shelves. Thus, ice loss from the Antarctic ice sheet is primarily by melting from beneath, and iceberg calving from seaward ice fronts, of ice shelves.

By contrast, the Greenland climate is strongly affected by its proximity to other land masses and to the North Atlantic, with the Gulf Stream to the south and regions of North Atlantic deep water production to the east and west. Ice-core data from the summit of the ice sheet indicate that Greenland temperatures and accumulation rates can increase significantly over periods of a few years

to decades (Alley et al., 1993). Other major contrasts with Antarctica include widespread summer melting, higher accumulation rates, very few ice shelves, and faster, narrower glaciers. Summer melting occurs over about 50 % of the ice-sheet surface, depending on summer temperatures, with much of the resulting melt water flowing into the sea, either along channels cut into the ice surface or by draining to the bed via crevasses. Mass loss by surface melting accounts for about half the total ice loss from Greenland, with iceberg calving responsible for the rest. Most Greenland outlet glaciers are narrower, by an order of magnitude, than their Antarctic counterparts, but some reach speeds that are an order of magnitude higher. Consequently, these glaciers drain very large volumes of ice, with discharge rates strongly determined by fast-glacier dynamics, which are poorly understood.

The polar ice sheets are remote, difficult to visit, and easily regarded as being of little significance to the rest of the world. But in two ways, they have turned out to be of growing importance: They preserve a record of past climate and climate change, and they control global sea level.

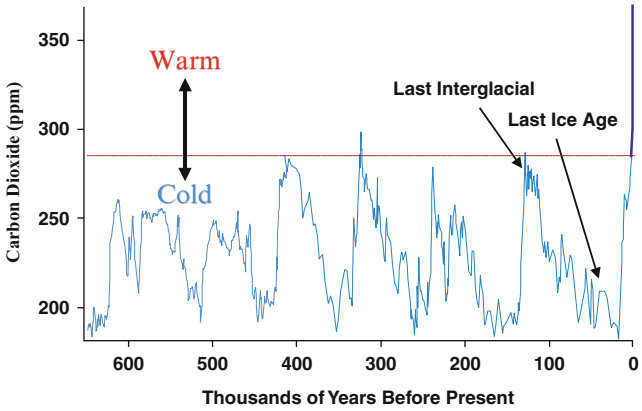

Ice Sheets and Ice Volume, Figure 5 Ice ages, represented by variations in atmospheric carbon dioxide preserved in ice cores, are "forced" by Earth's orbital clock, which changes the patterns of received sunlight. The big increase in carbon-dioxide concentrations over the past 100 years is shown by the *dark blue vertical line*.

Ice cores reveal a history of climate

Most of the surface of the Antarctic ice sheet, and about half of the Greenland ice sheet, is too cold for there to be much surface melting, and snow that falls on the ice sheets is slowly compressed until air that is trapped in the snow becomes isolated into small bubbles that shrink in size at increasing depths and finally dissolve in surrounding ice. Because there is little or no surface melting, annual layers of snow accumulation are unmixed with others, and they retain a signature of past climate, which can be sampled by drilling deep ice cores from cold parts of the ice sheet. The variety of climatic proxies in these cores is greater than in any other natural recorder of climate, such as tree rings or sediment layers. They include information on past ice-sheet surface temperatures and elevations, precipitation, chemistry and gas composition of the lower atmosphere, volcanic eruptions, solar variability, sea-surface productivity, desert extent, and forest fires.

Prevailing temperatures when the snow fell can be inferred from the ratios of different isotopes of oxygen and hydrogen in its water molecules. The ocean contains both normal and "heavy" water: Roughly one molecule in 500 includes at least one extra neutron in the nucleus of an oxygen or hydrogen atom. The lighter molecules evaporate more easily, and the heavier molecules condense more easily. Consequently, as water that evaporated from the ocean is carried inland over an ice sheet, the heavy molecules preferentially rain or snow out, leaving the lighter molecules to precipitate at colder temperatures. Calibration of the ratios of heavy versus light molecules in present-day snowfall against prevailing air temperatures allows interpretation of similar ratios in snow and ice recovered by the ice cores. Because of substantial differences between temperatures of summer and winter snowfall, annual layers can be counted down to considerable depths in regions of high snowfall, such as Greenland.

In the upper parts of a core, annual layers may also be visible, related to dustiness or summer-melt intensity. But deeper layers thin because of outward spreading of the ice sheet, and eventually individual years cannot be distinguished. Dating can also be inferred from the depths of events such as nuclear bomb fallout in the upper levels and ash layers corresponding to known volcanic eruptions. At greater depths, approximate dating can be estimated from radiocarbon or other radionuclide dating or by ice-flow modeling.

In addition to information from the isotope composition of the ice, the air bubbles and dust trapped in the ice cores allow for measurement of the atmospheric concentrations of dust and trace gases, including the greenhouse gases carbon dioxide, methane, and nitrous oxide. Total atmospheric concentration within the core at different depths indicates the air pressure, and hence surface elevation, at the time of snow deposition. Analysis of the dust and its concentration provides information on its source, and hence wind patterns, and on overall global dustiness. It also gives a strong indication of human influence on the concentration of atmospheric pollutants, such as lead and DDT. Greenhouse gas concentrations clearly show growth in these gases since the beginning of the Industrial Revolution, with a progressive acceleration in this growth as a burgeoning world population demands the fruits of affluence. Greenhouse gas concentrations are now higher than at any time during the 800,000 years covered by the ice-core record (Figures 5 and 6).

The length of the time record obtained by an ice core depends on the depth reached by the core and by the local snow-accumulation rate. It varies from a few years for

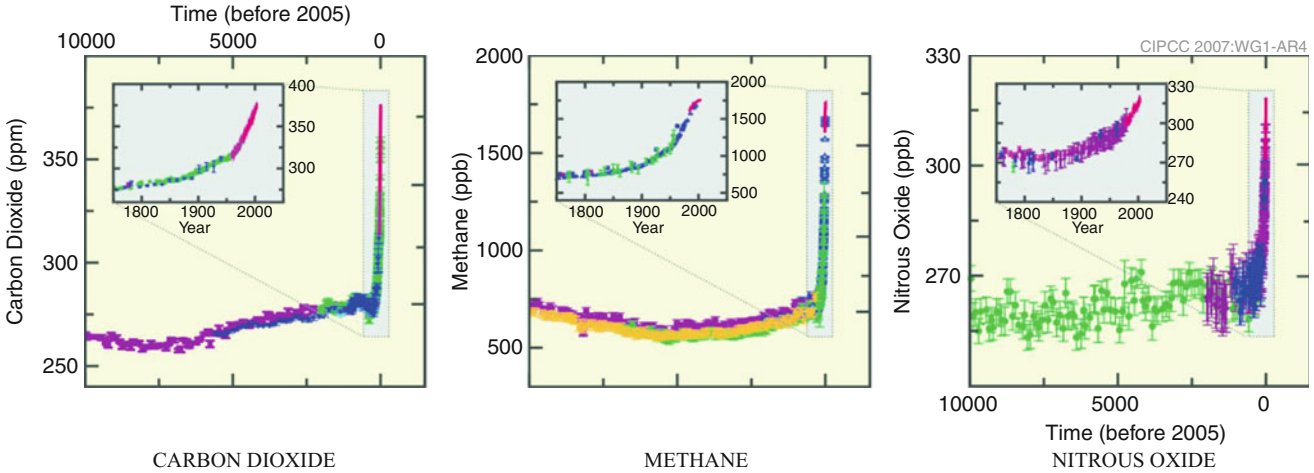

Ice Sheets and Ice Volume, Figure 6 Ice cores show these dramatic increases in greenhouse gases over the past 100 years as global energy consumption has increased.

a shallow core (typically 10 m) up to 800,000 year for the 3,200 m EPICA core in East Antarctica, which provides a climate record covering eight glacial cycles. The transition from glacial to interglacial conditions about 430,000 years ago resembles the transition into the present interglacial period in terms of the magnitude of change in temperatures and greenhouse gases. The interglacial that followed lasted 28,000 years compared to the 12,000 years recorded so far in the present interglacial period. Given the similarities between this earlier warm period and today, this may imply that, without human intervention, a climate similar to the present one would extend well into the future.

Although ice cores have revealed much about the growth and collapse of past ice sheets, little was known about their present behavior until quite recently. The past two decades have seen a dramatic change in our ability to observe the ice sheets, made possible by advances in remote-sensing techniques and their application aboard aircraft and satellites.

Applications of remote sensing to ice-sheet investigations

The polar ice sheets are remote and inhospitable and, until the 1970s, observations were largely made in situ, supplemented by just a few air photographs. Consequently, little was known about their behavior apart from the very few locations where detailed measurements had been made. Snow accumulation was measured by repeated stake measurements or by interpreting snow layers in a pit or shallow drill core. Ice motion was measured by repeatedly surveying stake locations with respect to local fixed points, by sun or star observations where there were no fixed points, or by repeated mapping of local magnetic anomalies. Ice thickness was measured using seismic techniques. Progress was slow until, in the early 1970s, scientists at the Scott Polar Research Institute in Cambridge, England, developed a low-frequency airborne radar capable of penetrating ice and receiving a reflected signal from the ice bed. This made possible major ice-thickness surveys in both Antarctica and Greenland that advanced our knowledge substantially. Later in the same decade, NASA launched *SeaSat*, a near-polar orbiting satellite with various sensors aboard designed to observe the ocean but which also turned out to be remarkably well suited to observing the polar ice sheets.

Included aboard SeaSat were:

- A *passive-microwave* radiometer, which images microwave emissions from the surface. Passive-microwave data have been successfully applied to the mapping of surface melting on the ice sheets and can also be used to help interpolate estimates of snow-accumulation rates between in situ measurements (Figure 7).
- A *scatterometer*, which images microwave reflections from an onboard radar and maps areas with near-surface ice layers in addition to those with surface melting.
- A *synthetic aperture radar* (SAR), which records the time delay, the phase, and the amplitude of reflections from a side-looking radar. In addition to providing high-resolution, all-weather images of glaciers and ice sheets, the information from repeated SAR images of the same area can be used to reconstruct surface topography and to map accurate estimates of ice motion at high spatial resolution. This final capability transformed our ability to study the polar ice sheets.
- A *radar altimeter* that measures the closest range from the spacecraft to the surface beneath. Designed to measure ocean topography, this instrument was the first to provide estimates of ice thickening/thinning rates over

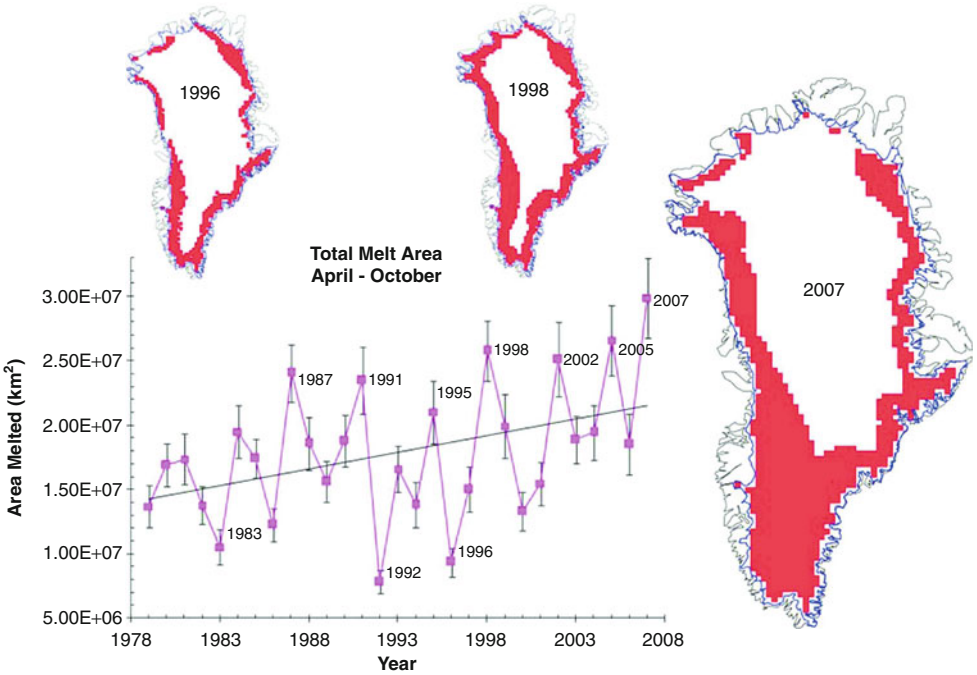

Ice Sheets and Ice Volume, Figure 7 The graph shows the total cumulative melt area from 1979 to 2007 for the Greenland ice sheet derived from satellite passive-microwave data. The map inserts display the area of melt for 1996, 1998, and the record year 2007 (From K. Steffen, CIRES, University of Colorado).

large regions. Unfortunately, however, the large radar beam width and the possibility of radar penetration below the ice-sheet surface make accurate interpretation very difficult.

All of these sensors clearly demonstrated the enormous potential of satellite remote sensing for ice-sheet research and have been included on various other spacecraft since. Together, they have revolutionized the study of the polar ice sheets. They have also helped focus in situ measurements by identifying regions where such measurements may be most productive. Nevertheless, some measurements are best made from aircraft, particularly after the availability for civil applications of the *Geodetic Positioning System* (GPS) in the early 1990s made it possible to reconstruct very accurately an aircraft trajectory and to follow earlier aircraft routes during repeat surveys. This capability made it possible, starting in 1991, for NASA to make accurate measurements of ice-surface elevations (to within +/− 10 cm), using a scanning laser altimeter along several tens of thousands of km of flight tracks over the Greenland ice sheet. Repeat surveys in 1993 and 1998 provided the first indication that the ice sheet was losing mass overall, with slow central thickening more than balanced by far more rapid thinning nearer the coast. Ice thickness was also measured along these flight lines, providing information needed to interpret observed thickening/thinning rates, information that cannot yet be acquired from satellite-borne sensors. Unfortunately, the remoteness and sheer size of Antarctica prevented similar surveys over the Antarctic ice sheet.

Later, in 2003, NASA launched the Geoscience Laser Altimeter System (GLAS) aboard the near-polar orbiting *ICESat* to make similar measurements over both ice sheets and the rest of Earth's surface. Unfortunately, problems with the laser system resulted in reducing its use to two or three surveys per year, each lasting about a month. The laser finally ceased operating in 2009. Data from ICESat confirmed the overall pattern of slow thickening over parts of central Greenland and rapid thinning over many coastal regions and revealed patterns of elevation change over Antarctica. However, cloud cover and the quite large separation between adjacent ICESat orbits resulted in incomplete coverage of the ice sheets, particularly in coastal regions where thinning rates are highest (Figure 8).

A joint NASA/German Aerospace Center (DLR) mission, the Gravity Recovery and Climate Experiment (*GRACE*), launched in 2002 and expected to continue operating until 2015, maps Earth's gravity field by precisely measuring the time-varying distance between two small satellites chasing each other along a near-polar orbit. Temporal changes in the gravity field result from mass shifting over, and beneath, the Earth's surface, including

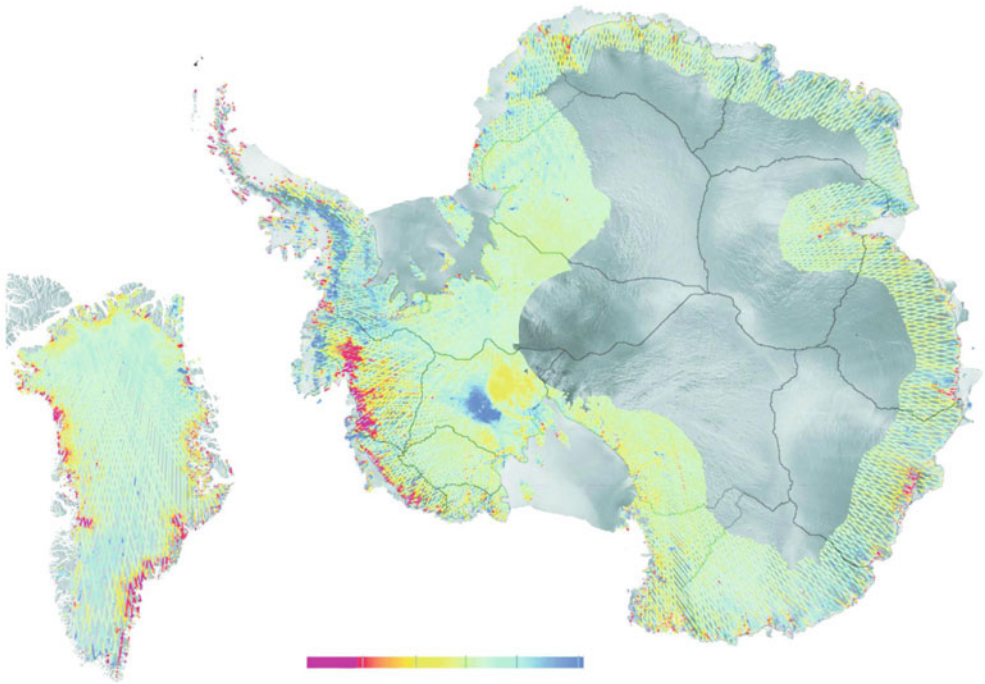

Ice Sheets and Ice Volume, Figure 8 Rate of change of surface elevation for Antarctica and Greenland; the color scale shows rates of elevation change ranging from thinning of 1.5 m/year (*purple*) to thickening of 0.5 m/year (*blue*) (Pritchard et al., 2009).

the changing mass, of the polar ice sheets. Results have been widely used to infer changes in ice mass or total mass balance integrated over very large areas.

Until quite recently, the ice sheets were assumed to be approximately in *steady state*, with total snow accumulation roughly in balance with total losses by melting and ice discharge. This was not based on measurements of these parameters, but rather on very low rates of observed sea-level rise (SLR) – close to only 1 mm/year – implying very small changes in ice-sheet volume. But measuring and understanding the mass balance of the Greenland and Antarctic ice sheets and of individual drainage basins within the ice sheets have long been major goals of ice-sheet science, and the satellite and aircraft measurements described above resulted in major advances toward these goals. Fortuitously, these advances came at a time when SLR rates began to increase substantially. If the polar ice sheets were to melt completely, global sea level would rise by about 64 m, so measuring and understanding their mass balance help to explain the recent increase in SLR and to predict future SLR.

Measuring the mass balance of the polar ice sheets

Techniques for measuring total mass balance of the polar ice sheets include:

- *The mass-budget approach*, comparing gains by surface and internal accumulation with losses by ice discharge, sublimation, and melt-water runoff. Snow accumulation is estimated from stake measurements, annual layering in ice cores, or from regional atmospheric climate modeling. Ice discharge is the product of velocity and thickness, with velocities measured by ground-based survey, photogrammetry, or, increasingly, with satellite SAR operating interferometrically, and thickness generally measured by airborne radar. Melt-water runoff is inferred from regional atmospheric climate models validated with surface observations where available. Mass-budget calculations involve the comparison of two very large numbers, and small errors in either can result in large errors in estimated total mass balance.
- *Repeated altimetry surveys*, to measure height changes, from which changes in volume and mass are inferred. Rates of surface-elevation change with time (dS/dt) reveal changes in ice-sheet mass after correction for changes in depth/density profiles and vertical bedrock motion. Satellite radar altimetry has been widely used, but data interpretation is difficult because of time-variable radar penetration into the snow and, over sloping and undulating surfaces, because of the large radar footprint. These limitations are overcome by laser altimetry, but problems with NASA's ICESat resulted in a comparatively sparse data set that poorly reveals the behavior of individual glaciers and ice streams, which are better investigated using airborne laser altimetry, with the added advantage of providing an opportunity to measure ice thickness at the same time. All altimetry mass-balance estimates include substantial uncertainties associated with settling of surface snow

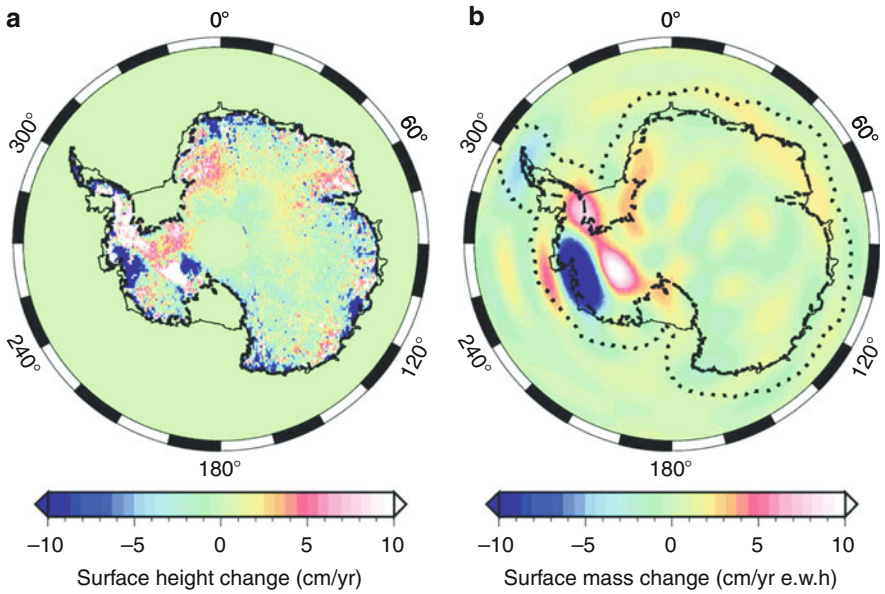

Ice Sheets and Ice Volume, Figure 9 Estimates of rates of surface-elevation changes from ICESat (**a**), and mass changes from GRACE represented as equivalent water depth changes (**b**) (Riva et al., 2009).

and with density assumed to convert thickness changes to mass changes.

- *Satellite measurements of temporal changes in gravity*, to infer mass changes directly. Since 2002, the GRACE satellite has measured Earth's gravity field and its temporal variability. After removing the effects of tides, atmospheric loading, spatial and temporal changes in ocean mass, etc., high-latitude data contain information on temporal changes in the mass distribution of the ice sheets and underlying rock. Mass-balance estimates are – at coarse resolution – several hundred kilometers, but this has the advantage of covering entire ice sheets, which is extremely difficult using other techniques. Consequently, GRACE estimates include mass changes on the many small ice caps and isolated glaciers that surround the big ice sheets, which are strongly affected by changes in the coastal climate. Error sources include measurement uncertainty, leakage of gravity signal from regions surrounding the ice sheets, and causes of gravity changes other than ice-sheet changes. Of these, the most serious are the gravity changes associated with vertical bedrock motion (Figure 9).

Mass balance of the Greenland and Antarctic ice sheets

Most model results previously suggested that climate warming would result primarily in increased melting from coastal regions and an overall increase in snowfall, with probably a small mass loss from Greenland and a small gain in Antarctica during the twenty-first century, and little combined impact on sea level. But recent measurements using the techniques described in the last section show substantial losses from both ice sheets but with poor agreement between estimates from the three different techniques. Moreover, each technique is under continual development and improvement, so that estimates based on the same set of measurements are continually changing. Nevertheless, the three independent techniques for estimating mass balance do provide the means for cross-checking results, and they increase our confidence in results where there is general agreement.

Available results indicate that annual ice loss from the Greenland ice sheet during the period with good observations increased from a few tens of cu km in the mid-1990s to perhaps as much as 200 cu km for the most recent observations. Near-coastal summer melting has increased substantially, but this is largely balanced by increased snowfall further inland, and an increasing proportion of the ice loss is by enhanced ice discharge down accelerating glaciers. Over the same period, net loss from Antarctica increased from probably near zero in the mid-1990s to nearly 100 cu km/year since 2000, almost entirely because of increased ice discharge along accelerating glaciers in West Antarctica and the Antarctic Peninsula (Figures 10–12).

Dynamic response of outlet glaciers to ice-shelf breakup

Recent rapid changes in marginal regions of both ice sheets include regions of glacier thickening and slowdown

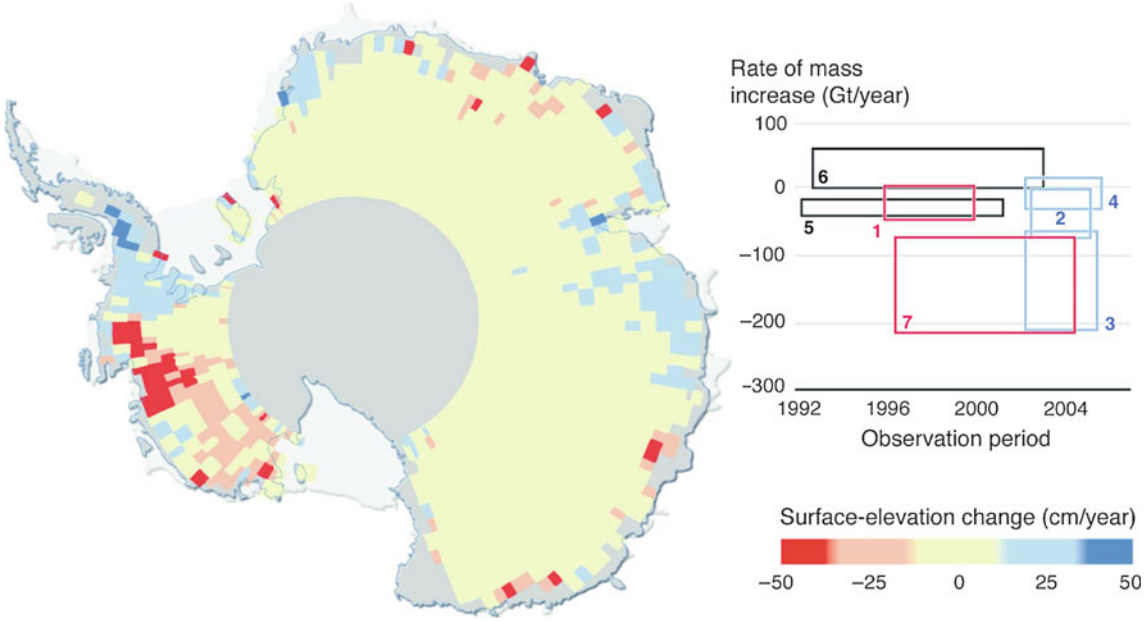

Ice Sheets and Ice Volume, Figure 10 Antarctica, showing rates of surface-elevation change derived from satellite radar-altimeter measurements. The graph on the *right* shows rates at which the ice-sheet mass was estimated to be changing based on radar-altimeter data (*black*), mass-budget calculations (*red*), and satellite gravity measurements (*blue*). Rectangles depict the time periods of observations (*horizontal*) and the upper and lower estimates of mass balance (*vertical*). Note that an ice loss of about 360 Gt/year (=400 km^3/year) raises sea level by 1 mm/year (Figure compiled by R. Thomas and S. Manizade).

but mainly acceleration and thinning, with speeds of some glaciers more than doubling. Most of these accelerations closely followed reduction or loss of ice shelves. Such behavior was predicted 40 years ago by John Mercer, based on evidence left by previous ice ages, and by Terry Hughes, based on the surface profiles of existing glaciers flowing into the Ross Ice Shelf. Soon after, Bob Thomas found evidence for the buttressing effects of ice shelves in his measurements of ice-shelf spreading rates. But the suggestion was discounted by most glaciologists as recently as the Third IPCC Assessment Report on Climate Change in 2001, based largely on results from prevailing model simulations. Soon after this, however, total breakup of the floating ice tongue of Jakobshavn Glacier in Greenland, preceded by its very rapid thinning and followed by doubling of the glacier velocity to 14 km/year, clearly showed the sensitive link between floating ice shelves and the glaciers that flow into them (Figure 13).

Most ice shelves are in Antarctica, where they cover an area of about 1.5 million sq km with nearly all ice streams and outlet glaciers flowing into them. Several small ice shelves on the Antarctic Peninsula collapsed in the last three decades of the twentieth century, possibly related to local atmospheric warming of about 3 °C over the second half of the twentieth century. Most of these ice-shelf breakups were closely followed by large accelerations of tributary glaciers, confirming the predictions discussed above. Based on these observations, it appears that ice shelves become vulnerable to breakup if mean annual air temperature exceeds −5 °C. It is also probable that ocean warming preconditions an ice shelf for breakup by thinning the ice shelf as basal melting increases, and the very rapid thinning of the Jakobshavn floating ice tongue coincided with inflow of very warm ocean waters into the glacier's fjord.

Outlook: the future

Model results predict increasing snowfall in a warming climate in Antarctica and Greenland, but only the latter has been verified by independent measurements. These studies also show significantly increased melt-water runoff from Greenland in a warming climate, partly compensated by the increased snowfall, and data from recent years suggest an increase in net loss from the surface mass balance. Consequently, because there is summer melting over ~50 % of Greenland already, and a small temperature rise substantially increases the area of summer melting, the ice sheet is particularly susceptible to continued warming. Model studies indicate that

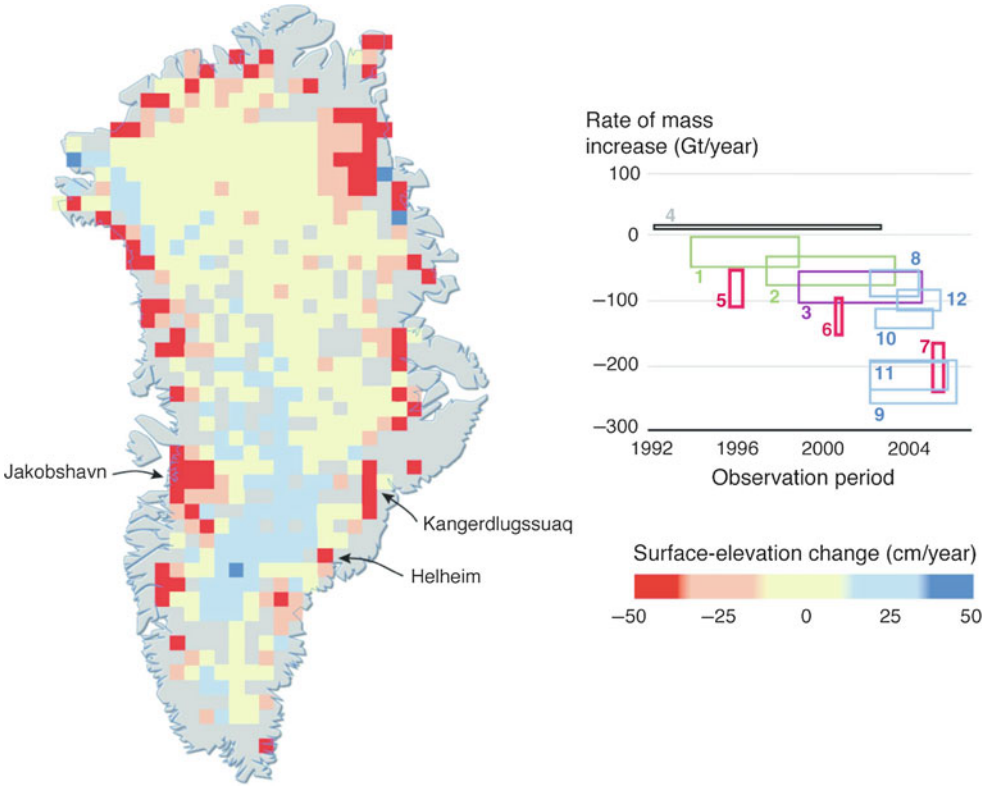

Ice Sheets and Ice Volume, Figure 11 Greenland, showing rates of surface-elevation change between the late 1990s and 2003, derived by comparing satellite and aircraft laser-altimeter surveys. The graph shows rates at which the ice-sheet mass was estimated to be changing based on satellite radar-altimeter data (*black*), laser-altimeter surveys (*green* and *purple*), mass-budget calculations (*red*), temporal changes in gravity (*blue*). Jakobshavn, Helheim, and Kangerdlugssuaq are fast glaciers that doubled in speed recently (Figure compiled by R. Thomas and S. Manizade).

a temperature increase over Greenland by more than 3 °C would probably result in irreversible loss of the ice sheet. Moreover, this estimate is based on imbalance between snowfall and melting, and ice loss would be accelerated by changing glacier dynamics of the type we are already observing.

Although Greenland glacier tongues and ice shelves are vulnerable to ocean warming, there are few of them, most flow in deep troughs for only short distances inland, and central parts of the ice sheet are well protected by the fringe of near-coastal mountains. Antarctic Peninsula ice shelves are also small with comparatively little ice flowing into them, so their collapse has negligible impact on global sea level. Moreover, the largest ice shelves, in the Weddell and Ross Sea Embayments, are far to the south where it is considerably colder than the −5 °C viability criterion cited above. Much of the ice draining from the West Antarctic ice sheet flows into these two ice shelves, with the remainder flowing into the Amundsen Sea to the north. Here, by contrast, the ice shelves are quite small and many have been thinning over the past decade or more, with associated acceleration of tributary glaciers that flow along very deep troughs. In particular, the speed of *Pine Island Glacier* has roughly doubled since the 1970s, as its ice shelf thinned by as much as 5 m/year. This is a very large glacier, currently discharging more than 100 km^3 ice/year into the ocean – approximately double its "balance" value. Nearby glaciers have also accelerated, and this region is probably the most vulnerable in Antarctica to climate warming particularly if, as appears likely, this is accompanied by ocean warming.

The regions likely to experience future rapid changes in ice volume are those where ice is grounded well below sea level such as the West Antarctic ice sheet and large glaciers in Greenland like Jakobshavn Isbrae that flow into the sea through a deep channel reaching far inland. The interaction of warm ocean waters with the calving fronts and floating extensions of these glaciers represents a strong potential cause of abrupt change in the big ice sheets, and future changes in ocean circulation and ocean temperatures will very probably produce changes in ice-shelf basal melting, but the magnitude of these changes cannot currently be modeled or predicted. Moreover, calving, which can originate in fractures far back from the ice front, and ice-shelf breakup are very poorly understood. Inclusion of these processes in models will certainly yield sea-level projections

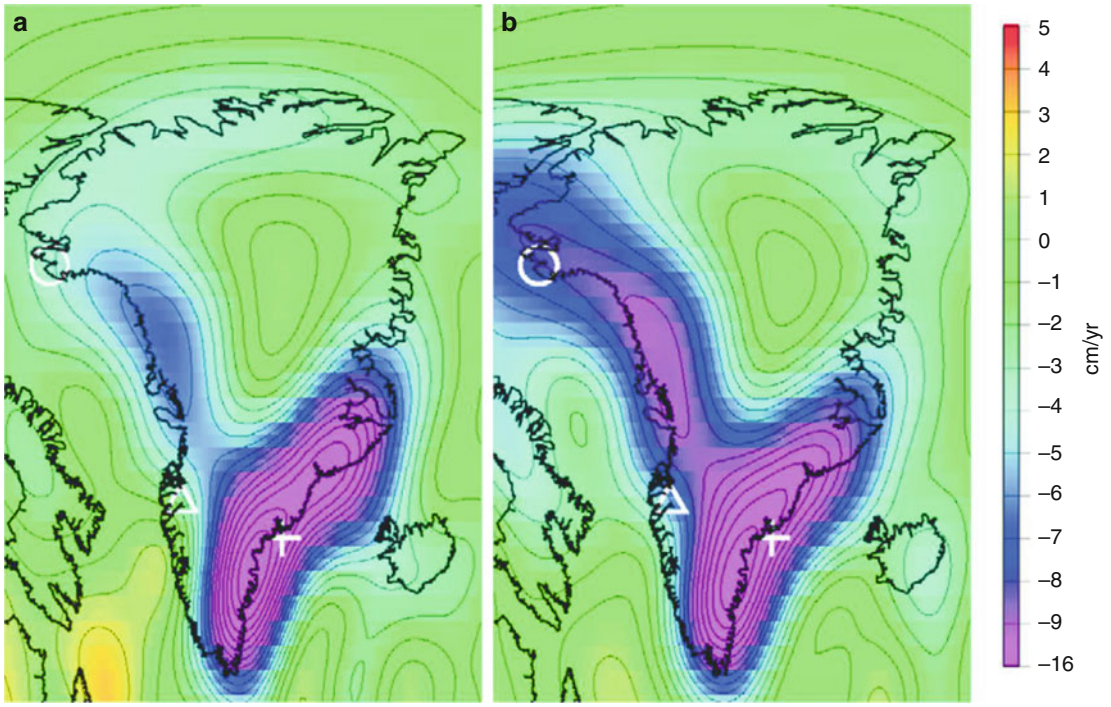

Ice Sheets and Ice Volume, Figure 12 The rate of mass loss, in cm/year water equivalent thickness, determined from monthly GRACE gravity field solutions. (**a**) The rate averaged between February 2003 and February 2007. (**b**) The rate averaged between February 2003 and June 2009 (Khan et al., 2010).

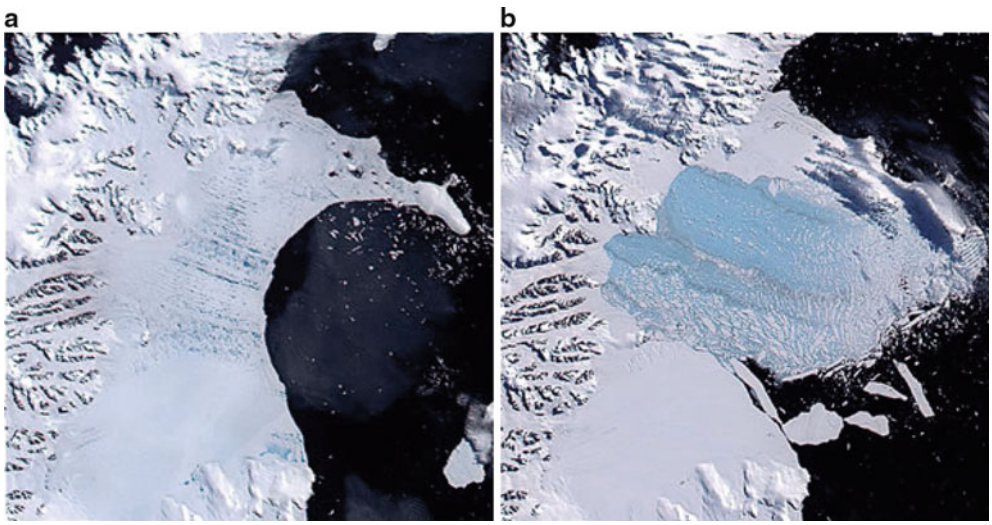

Ice Sheets and Ice Volume, Figure 13 Breakup of the Larsen B ice shelf. These are images from NASA's MODIS satellite sensor. Part of the Antarctic Peninsula is on the *left*. The image on the *left* (**a**) shows the shelf in late summer, with dark bluish melt ponds on the surface. The image on the *right* (**b**), collected only 5 weeks later, shows a large part of the ice shelf has collapsed, with thousands of sliver icebergs at the margins and a large blue area of ice fragments (Images: National Snow and Ice Data Center, Boulder, Colorado).

for the end of the twenty-first century that substantially exceed the projections presented in 2007 as part of the Fourth IPCC Assessment of Climate Change Report (0.28–0.42 m/year rise in sea level).

Bibliography

Alley, R., et al., 1993. Abrupt increase in snow accumulation at the end of the Younger Dryas event. *Nature*, **362**, 527–529.
Allison, I., et al., 2009. Ice sheet mass balance and sea level. *Antarctic Science*, **21**(5), 413–426.
Bentley, C., et al., 2007. Ice sheets. In *Global Outlook for Ice and Snow*. Nairobi: United Nations Environment Programme, pp. 99–113.
Khan, S. A., et al., 2010. Spread of ice mass loss into Northwest Greenland observed by GRACE and GPS. *Geophysical Research Letters*, **37**, L06501, doi:10.1029/2010GL042460, 2010.
Pritchard, H. D., et al., 2009. Extensive dynamic thinning on the margins of the Greenland and Antarctic ice sheets. *Nature*, doi:10.1038/nature08471.
Riva, E. M., et al., 2009. Glacial isostatic adjustment over Antarctica from combined ICESat and GRACE satellite data. *Earth and Planetary Science Letters*, **288**, 516–523.

ICEBERGS

Donald L. Murphy
International Ice Patrol, US Coast Guard,
New London, CT, USA

Synonyms

Glacier berg; Glacier ice; Ice island

Definition

Iceberg. A floating ice mass extending more than 5 m above the sea surface, which has calved from a glacier or ice shelf (World Meteorological Organization, 2007).
Ice shelf. A thick sheet of floating ice attached to land or a glacier (World Meteorological Organization, 2007).

Introduction

Long before *RMS Titanic* struck an iceberg and sank in the North Atlantic in April 1912, mariners were well aware of the beauty and danger icebergs present. The first documented iceberg report might have been provided as long ago as the sixth century by the legendary Irish monk, St. Brendan, who reported encountering floating crystal palaces during his North Atlantic voyage. It was *Titanic*, however, that brought a sense of urgency to tracking icebergs and distributing that information to mariners, a task that was assigned to the US Coast Guard International Ice Patrol (IIP). Despite impressive technological advances in shipboard radars, electronic navigational systems, and communications, ships still collide with ice. In November 2007, the cruise ship *MS Explorer* sank 20 h after striking ice off King George Island, near Antarctica. Fortunately, there was no loss of life. While it is not entirely clear whether *Explorer* struck sea ice or an iceberg, it is clear that the danger ice poses to ships is unabated. This threat extends to other offshore activities, such as oil production and exploration. For example, during the 2008 iceberg season in the western North Atlantic, a large number of icebergs threatened offshore oil platforms near Newfoundland, Canada. Production stopped for several days, and an exploratory drill rig suspended operations and departed the iceberg danger area.

Aside from the clear menace of icebergs to maritime safety, other reasons to examine iceberg populations include their role in mass balance and freshwater flux. Ice discharge is an integral part of ice-sheet mass balance. For instance, giant (>18.5 km long) icebergs calved from the Antarctic ice shelves and glacier tongues accounted for approximately half of the mass lost by the Antarctic ice sheet during the last 25 years (Silva et al., 2006). In the Arctic, the 2005 calving of a 66.4 km^2 ice island from the Ayles Ice Shelf, on Ellesmere Island, Canada (Copeland et al., 2007), reduced the area of the remaining Ellesmere ice shelves by about 7.5 %. Further, the subsequent melting of the calved icebergs contributes to the flux of freshwater to the ocean. The meltwater from the giant icebergs calved from Antarctica was shown to be significant in the Southern Ocean's freshwater balance and exceeded precipitation minus evaporation (P − E) in the Weddell Sea (Silva et al., 2006). Large icebergs also have the potential to alter the dynamics of the marine ecosystem substantially (Arrigo et al., 2002).

The earliest data on icebergs were obtained from ships. These include the extensive dataset collected by the Australian and Russian vessels in the Indian and Atlantic sectors of the Southern Ocean (Jacka and Giles, 2007; Romanov et al., 2008), the pre-World War II part of IIP's western North Atlantic iceberg dataset (IIP, 1913–1946), as well as others. The vast extent and isolated nature of the ocean regions populated by icebergs make extensive and frequent shipboard observations impractical; thus, the wide array of satellite-borne, airborne, and surface-based remote sensing instruments is particularly attractive in undertaking iceberg studies.

Iceberg properties and sizes

An iceberg is a floating ice mass extending more than 5 m above the sea surface (World Meteorological Organization, 2007). It may originate from a glacier flowing directly to the sea, such as the tidewater glaciers of Greenland (e.g., Joughin et al., 2004), or from an ice shelf. An ice shelf is a thick sheet of floating ice attached to land or a glacier (World Meteorological Organization, 2007). It may be nourished by snow falling directly on its surface. The large icebergs that calve from Antarctic ice shelves are usually referred to as tabular icebergs, while the term "ice island" is more commonly used to describe icebergs from Arctic ice shelves.

Icebergs, Table 1 Iceberg size categories used in the western North Atlantic and the Antarctic

North Atlantic (Environment Canada, 2005)			Australian Antarctic Program (Jacka and Giles, 2007)	
Description	Height (m)	Length (m)	Category	Length (m)
Growler	<1	<5	1	25–100
Bergy bit	1 to <5	5 to <15	2	100–200
Small iceberg	5–15	15–60	3	200–400
Medium iceberg	16–45	61–120	4	400–800
Large iceberg	46–76	121–200	5	800–1,600
Very large iceberg	>75	>200	6	1,600–3,200
			7	>3,200

Depending on their source, icebergs may have slightly differing compositions. The icebergs calved from Greenland's glaciers tend to be mostly glacial ice, with a density approximately that of pure ice (917 kg/m^3). Thus, approximately one-seventh of the mass of the iceberg will be above the ocean's surface (Lewis et al., 1994). The large tabular icebergs calved from Antarctic ice shelves are covered in snow, which reduces their mean density (Weeks and Mellor, 1978).

Icebergs come in a remarkable array of shapes with sizes spanning the range from a piano to a Caribbean Island. The sail height and keel depth of icebergs can vary widely depending on the shape of the iceberg. Typical freeboard heights for the large tabular icebergs calved from the major Antarctic ice shelves are 30–40 m (Jacka and Giles, 2007), while icebergs in the North Atlantic may reach heights of 100 m or more.

Iceberg length is a dominant factor in selecting the appropriate remote sensing system. The Canadian Ice Service (CIS) and IIP use a size classification scheme (Table 1) that is tailored for the icebergs entering the busy shipping lanes in the western North Atlantic Ocean. It reflects the fact that small pieces of ice can severely damage a vessel. An iceberg exceeding just a few kilometers in length is very rare. This classification scheme is wholly inadequate for the massive icebergs found near Antarctica. Although there is no universally accepted size classification scheme for Antarctic icebergs, the one used by the Australian Antarctic Program (Table 1) accounts for a wider range of large icebergs. To further emphasize the size disparity, an Antarctic iceberg must measure at least 18.5 km along the long axis to be entered into the United States (US) National Ice Center's (NIC) iceberg database (NIC, 2008).

Using remotely sensed information to study icebergs

Both passive and active sensors have been used successfully in iceberg studies. Passive sensors, which rely on natural illumination and emission, include visual and infrared systems and passive microwave sensors. Active sensors, which provide their own illumination, include radar systems such as radar altimeters and imaging radars. Each has advantages and disadvantages for areal coverage, spatial and temporal resolution, and the ability to provide data irrespective of weather and light conditions. The following discussion describes a few of the sensors that have provided remotely sensed data to advance the knowledge of the distribution and behavior of icebergs. It focuses on satellite-borne instruments because of their ability to cover wide areas, a significant advantage when monitoring icebergs. The discussion includes some of the inevitable trade-offs between resolution, an indicator of the iceberg length that can be detected, and areal coverage (swath) of the instrument. For some of the instruments, the polarization of the signal is also an important characteristic. This is particularly significant to the ability of synthetic aperture radars (SAR) to distinguish between icebergs and vessels.

Visual and infrared sensors

Satellite-borne visual and infrared sensors, such as the Advanced Very High Resolution Radiometer (AVHRR) on the National Oceanic and Atmospheric Administration's (NOAA) polar-orbiting satellites and the Operational Linescan System (OLS) on the Defense Meteorological Satellite Program (DMSP) satellites, are major sources of the NIC database of giant (>18.5 km in length) Antarctic icebergs (Long et al., 2002). This database has been used in numerous studies of Antarctic iceberg populations including an examination of the contribution of giant icebergs to the freshwater flux to the Southern Ocean (Silva et al., 2006). The nominal spatial resolution of the AVHRR is 1.1 km (NOAA, 1998), while the OLS fine-mode resolution is 0.55 km (NOAA, 2008). In both cases, the resolution is well suited to monitoring large icebergs in the Antarctic. The data are of relatively low cost and are available in near real time. Unfortunately, clouds and low-light conditions during the polar winter often hamper visual and infrared sensors, which may result in data gaps.

Passive microwave systems

Because they operate in the microwave range, passive microwave systems penetrate most clouds giving them a major advantage over the visible and infrared sensors. The 85 GHz channel on the special sensor microwave imager (SSM/I) on the DMSP satellite has been used to track large Antarctic icebergs (Hawkins et al., 1991). With a 16 km by 14 km footprint, this SSM/I channel is capable of detecting icebergs of several tens of km in length and larger.

The Advanced Microwave Scanning Radiometer (AMSR-E) on the Aqua satellite, launched in 2002 and functioned until 2011, was a significant improvement over SSM/I, particularly because it has much-improved spatial

resolution. The AMSR-E's 89 GHz channel had a much smaller footprint (6 km by 4 km), allowing it to detect smaller icebergs. It has been used to track 10 km icebergs in the Antarctic (Blonski and Peterson, 2006). As with the visual and infrared sensors, passive microwave sensors are adequate for tracking the large icebergs of the Antarctic but have limited use for iceberg tracking in the northern hemisphere.

Active microwave systems

Active microwave systems are becoming the dominant remote sensing instruments in the study of icebergs in both hemispheres. They include radar scatterometers and imaging radars. Many of the instruments offer finer resolution than visual, infrared, and passive microwave systems. More importantly, these systems provide their own illumination and are not weather dependent.

Radar scatterometers were designed to measure winds over the ocean from space, but because of the high radar backscatter of icebergs, they are useful for iceberg tracking as well. The spatial resolution varies according to the specific instrument but ranges from 2.225 to 8.9 km/pixel (Long et al., 2002). The data from five scatterometers were used to study the Antarctic iceberg population continuously from 1992 by Ballantyne and Long (2002). They suggest that the increase in the number of Antarctic icebergs observed in recent years is due to the improved detection and tracking technology. Stuart et al. (2008) maintain an online database of the iceberg locations derived from the scatterometer data.

The 1978 launch of the US National Aeronautics and Space Administration's (NASA) SEASAT ushered in the era of ocean-observing synthetic aperture radars (SAR). Although SEASAT provided data for only a few months, it paved the way for a progression of SAR satellites used to monitor icebergs over a wide range of sizes in both hemispheres. Since the early 1990s, imaging radars launched by the European Space Agency (ESA), the Canadian Space Agency (CSA), and others have become increasingly capable and flexible. These instruments offer numerous beam modes with various swaths and resolutions, some with the ability to detect 30 m icebergs (Power et al., 2001). The all-weather capability and wide range of iceberg sizes that can be detected make satellite-borne SARs valuable for both operations and research.

Because small icebergs pose the greatest threat to ships, the ability to detect them is particularly significant to maritime-safety operations. Such icebergs are large enough to inflict serious damage, yet small enough to elude detection in high sea states. Two challenges dominate the operational use of SARs to detect icebergs: first, the trade-off between resolution and coverage (swath) and, second, the ability to distinguish between icebergs and vessels. CSA's RADARSAT-1 is a single-polarization radar. For high incidence angles (>35°), it detects icebergs on the order of the resolution of the particular SAR mode. For example, in one mode, which has a 150 km swath, icebergs 30 m or larger can be detected (Power et al., 2001). In another mode, the swath increases to 300 km, but the resolution becomes 50 m. Single-polarization images do not always provide reliable ability to distinguish between ships and icebergs. The alternating polarization mode on the Advanced SAR (ASAR) on ESA's ENVISAT, launched in 2002, permits analysis of different polarization responses of ships and icebergs (Howell et al., 2004). The increased flexibility of choosing the signal polarization offered by the RADARSAT-2 improves the discrimination skills (Scheuchl et al., 2004).

Satellite-borne SAR data are providing a rich source of information for the study of iceberg populations throughout the world's oceans. In addition, because they are capable of detecting a wide range of sizes, they give a better representation of the populations. For example, the SARs on ESA's European Remote Sensing Satellites (ERS-1, ERS-2) and RADARSAT-1 were used to study the iceberg distribution in the Eurasian Arctic. Icebergs present there are much smaller than the Antarctic, with an average size of about 100 m. SAR images showed significant iceberg production from the Renown Glacier in Franz Josef Land (Alexandrov et al., 2003). SAR data in the Antarctic have provided another resource for the extensive iceberg database being maintained at the NIC (National Ice Center, 2008).

Two trends are emerging from the identification and tracking of icebergs using SAR data. First, the data sets are becoming so large that automated systems are required to conduct consistent and efficient analysis. Computer-based techniques have been developed to locate and identify Antarctic icebergs using SAR images (Silva and Bigg, 2005), and the system also retains the iceberg shape to facilitate tracking using sequential images. Second, the process of interpreting SAR images sometimes leads to ambiguities. For example, distinguishing between small icebergs and small multiyear sea ice floes can be difficult even for a skilled analyst. Small icebergs and small vessels are also difficult to distinguish.

Summary

The last few decades have witnessed remarkable improvements in the ability of satellite-borne sensors to detect, track, and measure icebergs of wide size range. The earliest capability was limited to detecting large Antarctic icebergs in favorable weather and light conditions. Now, numerous sensors, many unencumbered by weather and light conditions, are used in both hemispheres to track icebergs as small as a few tens of meters.

An enormous increase in the amount of available data, particularly from SARs, has led to the development of automated image-analysis techniques to detect icebergs. While many of these systems have proven successful, it is widely agreed that the human analyst cannot yet be removed entirely from the process. In addition, there is still much work to be done comparing remotely sensed data with surface observations.

Finally, it is likely that human activity in ice-populated waters will increase due to resource exploitation in the ice-diminishing Arctic and growing public interest in ecotourism. This will create new challenges for many of the world's operational ice centers. Today, 20 countries (World Meteorological Organization, 2006) have organizations that provide ice services. Their success at meeting future demands hinges on the effective and efficient use of remotely sensed data.

Bibliography

Alexandrov, V. Y., Sandven, S., and Kloster, K., 2003. Iceberg identification in the Eurasian Arctic using SAR images. In *Proceedings 2003 IEEE International Geoscience and Remote Sensing Symposium*, Vol. 4, pp. 2798–2801.

Arrigo, K. R., van Dijken, G. L., Ainley, D. G., Fahnestock, M. A., and Markus, T., 2002. Ecological impact of a large Antarctic iceberg. *Geophysical Research Letters*, **29**(7), 1104.

Ballantyne, J., and Long, D. G., 2002. A multidecadal study of the number of Antarctic icebergs using scatterometer data. In *Proceedings 2002 IEEE International Geoscience and Remote Sensing Symposium*, Vol. 5, pp. 3029–3031.

Blonski, S., and Peterson, C. A., 2006. Antarctic iceberg tracking based on time series of aqua AMSR-E microwave temperature measurements. *EOS, Transactions American Geophysical Union*, **87**(52), Fall Meeting Supplement, Abstract # IN33B–1352.

Copeland, L., Mueller, D. R., and Weir, L., 2007. Rapid loss of the Ayles ice shelf, Ellesmere island. *Canada Geophysical Research Letters*, **34**, L21501.

Environment Canada, 2005. *Manual of Standard Procedures for Observing and Reporting Ice Conditions (MANICE)*, 9th edn. Ottawa: Canadian Ice Service, Meteorological Service of Canada, Environment Canada.

Hawkins, J. D., Laxon, S., and Phillips, H., 1991. Antarctic tabular iceberg multi-sensor mapping. In *Proceedings 1991 International Geoscience and Remote Sensing Symposium, Remote Sensing: Global Monitoring for Earth Management*, Vol. 3, pp. 1605–1608.

Howell, C., Youden, J., Lane, K., Power, D., Randell, C., and Flett, D., 2004. Iceberg and ship discrimination with ENVISAT multi-polarization ASAR. In *Proceedings 2004 IEEE International Geoscience and Remote Sensing Symposium*, Vol. 1, pp. 113–116.

International Ice Patrol Annual Reports, 1913–1946. *International Ice Observation and Ice Patrol Service in the North Atlantic Ocean*. Bulletins 1–32. Groton, CT: U.S. Coast Guard International Ice Patrol.

Jacka, T. H., and Giles, A. B., 2007. Antarctic iceberg distribution and dissolution from ship-based observations. *Journal of Glaciology*, **53**(182), 341–356.

Joughin, I., Abdalati, W., and Fahnestock, M., 2004. Large fluctuations in speed on Greenland's Jakobshavn Isbrae glacier. *Nature*, **432**, 608–610.

Lewis, E. O., Livingstone, C. E., Garrity, C., and Rossiter, J. R., 1994. Properties of snow and ice. In Haykin, S., Lewis, E. O., Raney, R. K., and Rossiter, J. R. (eds.), *Remote Sensing of Sea Ice and Icebergs*. New York: Wiley.

Long, D. C., Ballantyne, J., and Bertoia, C., 2002. Is the number of Antarctic icebergs really increasing? *EOS Transactions American Geophysical Union*, **83**(42), 469.

National Ice Center, 2008. *Antarctic Icebergs*. Retrieved 13 June 2008 from http://www.natice.noaa.gov/products/iceberg/index.htm.

National Oceanographic and Atmospheric Administration, 1998. *NOAA Polar Orbiter data User's Guide*. Retrieved 14 June 2008 from http://www2.ncdc.noaa.gov/docs/podug/index.htm.

National Oceanographic and Atmospheric Administration, 2008. *DMSP Sensors*. Retrieved 14 June 2008, from http://www.ngdc.noaa.gov/dmsp/sensors.html.

Power, D., Youden, J., Lane, K., Randell, C., and Flett, D., 2001. Iceberg detection capabilities of RADARSAT synthetic aperture radar. *Canadian Journal of Remote Sensing*, **27**(5), 476–486.

Romanov, Y. A., Romanova, N. A., and Romanov, P., 2008. Distribution of icebergs in the Atlantic and Indian Ocean sectors of the Antarctic region and its possible links with ENSO. *Geophysical Research Letters*, **35**, L02506.

Scheuchl, B., Flett, D., Caves, R., and Cumming, I., 2004. Potential of RADARSAT-2 data for operational sea ice monitoring. *Canadian Journal of Remote Sensing*, **30**(3), 448–461.

Silva, T. A. M., and Bigg, G. R., 2005. Computer-based identification and tracking of Antarctic icebergs in SAR images. *Remote Sensing of Environment*, **94**(3), 287–297.

Silva, T. A. M., Bigg, G. R., and Nicholls, K. W., 2006. Contribution of giant icebergs to the Southern Ocean freshwater flux. *Journal of Geophysical Research*, **111**, C03004.

Stuart, K., Lambert, B., Ballantyne, J., and Long, D. G., 2008. *The Antarctic Iceberg Tracking Database, 1978 & 1992–2008*, Brigham Young University. Provo: UT. Retrieved 13 June 2008 from http://www.scp.byu.edu/data/iceberg/database1.html.

Weeks, W. F., and Mellor, M., 1978. Some elements of iceberg technology. In Husseiny, A. A. (ed.), *Iceberg Utilization, Proceedings First International Conference*. New York: Pergamon, pp. 45–98.

World Meteorological Organization, 2006. *Sea-Ice Information Services in the World*. WMO-No. 574, 3rd edn. Geneva: World Meteorological Organization. http://www.jcomm-services.org/documents.htm?parent=136.

World Meteorological Organization, 2007. Sea-ice nomenclature. *WMO Sea Ice Nomenclature*, draft, ver. 1.1. Geneva: World Meteorological Organization. http://www.jcomm-services.org/documents.htm?parent=136.

Cross-references

Ice Sheets and Ice Volume
Microwave Radiometers
Observational Systems, Satellite
Radar, Synthetic Aperture

INTERNATIONAL COLLABORATION

Lisa Robock Shaffer
MC 0553 Rady School of Management, University of California, San Diego, La Jolla, CA, USA

Synonyms

Bilateral or multilateral collaboration; International cooperation

Definition

A variety of forms of participation in remote sensing missions by organizations or individuals from more than one country. This includes space-based missions whose hardware includes components from different countries, as well as science team participation by persons

from countries other than the country of the Principal Investigator. International collaboration can also take the form of multilateral organizations in which program planning, education and outreach, calibration and validation, and other aspects of program coordination take place.

Introduction

International collaboration in remote sensing can take place in any or all elements of a typical mission: mission planning, spacecraft bus, instrument payload, launch vehicle, operations, data acquisition, and data analysis. From the simple sharing of an image acquired from space to the design of an integrated mission involving multiple partners, the history of space-based Earth observations provides examples of all levels of international engagement.

Data Sharing Across Borders: The simplest form involves someone in one country using data from a mission provided by another country. It can involve the transmission of data received centrally and distributed through terrestrial means (postal mail or electronic transmission). In the early history of Earth observations, this was typical – a magnetic tape or a copy of a photograph or other image would be created and shipped to an investigator in another country, after a competitive process of selecting a scientific research team through an international call for proposals. For some missions where there is interest in the data for purposes beyond the scientific objectives of the sponsoring agency, data have been provided on varying terms from no charge to cost of reproduction to commercial prices, sometimes without restriction and sometimes with very specific constraints on how the data could be used and by whom. Data from US weather satellites is the least restricted, and missions that have commercial dimensions such as SeaWiFS and SPOT have the most complex data access policies.

Data sharing can involve direct reception of data from one country's satellite received at a ground station in another country. The earliest form of such collaboration is probably the US weather satellites in the early 1960s. President Kennedy decreed that all the data would be openly transmitted on a global basis, and the US Government provided technical information and assistance to enable meteorological agencies around the world to receive data from the Automated Picture Transmission (APT) system. Data from NOAA satellites continues to be openly transmitted without a fee to this day, with technical support available through the World Meteorological Organization, to enable all nations, regardless of their economic status, to have vital weather information. A more complex version of this kind of cooperation continues today with remote sensing satellites including the US Landsat and French SPOT satellite series, in which ground station operators acquire data directly from the satellite but on a scheduled, fee-based arrangement.

Instrument Provision: Some satellite payloads include instruments provided by foreign space agencies. These can be selected through a competitive process where instrument providers submit proposals to the mission lead agency, such as was done for the original NASA Earth Observing Satellite platforms and NSCAT flying on ADEOS, or specific instrument contributions can be solicited from specific providers and negotiated on a bilateral basis, such as the Search and Rescue COSPAS/SARSAT packages that fly on the polar-orbiting meteorological satellites.

Joint Missions: When there is shared planning from the inception of a mission, we refer to the type of collaboration as a joint mission. The US-French Topex/Poseidon and JASON satellites are an example, as are missions undertaken by the European Space Agency and EUMETSAT, in which the member states develop the plans for both the jointly funded elements of the payload and any national contributions as part of the mission design from the start. The Tropical Rainfall Monitoring Mission, jointly developed by NASA and NASDA is another example.

Launch and Operations: Sometimes the international collaboration comes in the form of operations support, such as provision of a launch and support for operations. The Pegasus launch of an SAC mission for Argentina and the Ukraine launch vehicle provided for GRACE are examples. In both cases, the missions themselves are also international, SAC being a collaboration between NASA and CONAE (Argentina) and GRACE involving NASA and the German space agency, DLR.

Planning and Coordination: There are several international organizations that have played a critical role in stimulating international collaboration in remote sensing. These include the World Meteorological Organization (WMO), whose coordination of meteorology predates the existence of space-based observing systems and which has been essential in the expansion of international cooperation into the satellite era. The Coordination of Geostationary Meteorological Satellite (CGMS) group (which became the Coordination Group for Meteorological Satellites) was instrumental in developing payload harmonization and backup operational arrangements for the major geostationary weather satellite systems. The Committee on Earth Observation Satellites (CEOS) was established in 1984 and has provided a venue for technical working groups on such topics as sensor calibration and validation, data cataloging, and format standards, as well as regularly convening senior space agency officials to discuss long-range mission plans and coordinate educational outreach and develop advocacy strategies to secure and expand public support and funding for space-based Earth observations.

As a result of the work of these groups and others, in 2003 the first Earth Observation Summit was convened at ministerial level and established a process that has resulted in creation of the Global Earth Observing System of Systems (GEOSS) and the Group on Earth Observations (GEO), formed in 2005 to carry out the 10 year GEOSS implementation plan.

Summary

As the need to observe and understand the planet increases in importance, and as the recognition of our global interdependence grows, it is only natural that the advanced technologies used to observe the Earth from space would stimulate international collaboration in many forms. The technological and scientific challenges require the best and brightest from across the planet to address the critical challenges of climate change and sustainability.

Bibliography

Committee on Earth Observation Satellites (CEOS), http://www.ceos.org/
EUMETSAT, http://www.eumetsat.int/Home/index.htm
European Space Agency, Earth Observations, http://www.esa.int/
Group on Earth Observations (GEO), http://earthobservations.org/
NASA Office of External Relations, Science Division, http://www.hq.nasa.gov/office/oer/science.html
NOAA/NESDIS International and Interagency Affairs Office, http://www.noaa.gov/

Cross-references

Data Policies
Global Climate Observing System
Global Earth Observation System of Systems (GEOSS)
Global Land Observing System
Policies and Economics
Public-Private Partnerships
Remote Sensing, Historical Perspective

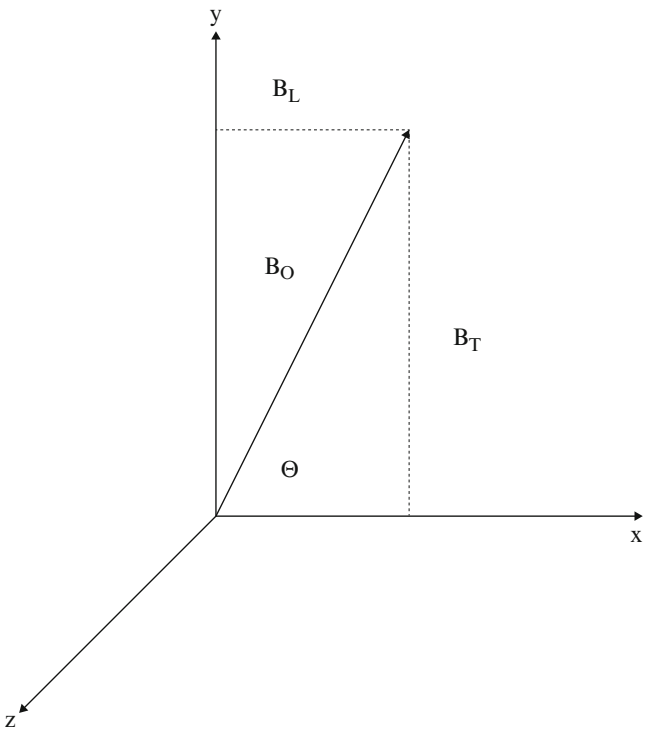

Ionospheric Effects on the Propagation of Electromagnetic Waves, Figure 1 System of orthogonal axes x, y, z (After Davies, 1990).

IONOSPHERIC EFFECTS ON THE PROPAGATION OF ELECTROMAGNETIC WAVES

Attila Komjathy
Jet Propulsion Laboratory, California Institute of Technology, Pasadena, CA, USA

Synonyms

Ionospheric wave specification or wave propagation; Propagation of electromagnetic waves in the ionosphere

Definition

- *Appleton-Hartree Formula*. the equation describing the medium that is electrically neutral with constant magnetic field impressed upon it.
- *Ground and Space-Based Remote Sensing Techniques*. instruments placed on the ground or onboard satellites measuring critical ionospheric parameters and integrated electron densities (i.e., total electron content or TEC).

Introduction to ionospheric propagation

The effect of the ionosphere on electromagnetic waves propagation (see "*Electromagnetic Theory and Wave Propagation*") can only partially be described by simple dispersion. To adequately describe the complete behavior of radio waves in the ionosphere, it is important to realize that the "ionosphere is a partially ionized, spherically stratified plasma with a wide spectrum of non-uniformly spaced irregularities, upon which is imposed a non-uniform magnetic field" (Hunsucker, 1991).

The complex refractive index of the ionosphere as a magnetoionic medium was derived by the number of scientists, but the name most commonly associated with the theory is Sir Edward Appleton who was first to point out that a plane-polarized wave would be split into two opposite rotating circularly polarized waves by the magnetized plasma (Hunsucker, 1991). In 1931, Hartree suggested the inclusion of the Lorentz polarization term after which event the complex refractive index was often referred to as the Appleton-Hartree formula.

The detailed derivation of the formula can be found in Davies (1966, 1990) and Komjathy (1997). First, we have to apply Maxwell's equations to the wave, and secondly we have to impose the properties of the medium, the so-called constitutive relations. *The Appleton-Hartree magnetoionic theory* applies to a medium that is electrically neutral with no resultant space charge and an equal number of electrons and positive ions upon which a constant magnetic field (see "*Earth Magnetic Field*") is impressed, and the effect of positive ions on the wave is

negligible. Let us consider a plane electromagnetic wave travelling in the x direction of the orthogonal coordinate system displayed in Figure 1.

Let us also consider a uniform external magnetic field that lies in the x-y plane and makes an angle θ with the - direction of propagation. The complex refractive index n is given by the Appleton-Hartree magnetoionic dispersion equation (see e.g., Langley, 1996; Davies, 1966, 1990; Hunsucker, 1991; Hall and Barclay, 1989):

$$n^2 = 1 - \frac{X}{(1-jZ) - \left[\frac{Y_T^2}{2(1-X-jZ)}\right] \pm \left[\frac{Y_T^4}{4(1-X-jZ)^2} + Y_L^2\right]^{1/2}}, \tag{1}$$

where n is the complex refractive index $(\mu - j\chi)$ with μ being the real part and χ being the imaginary part. Furthermore:

$$X = \frac{\omega_N^2}{\omega^2} = \frac{f_N^2}{f^2}, \tag{2}$$

$$Y = \frac{\omega_H}{\omega} = \frac{f_H}{f}, \tag{3}$$

$$Y_L = \frac{\omega_L}{\omega},\ Y_T = \frac{\omega_T}{\omega}, \tag{4}$$

$$Z = \frac{\omega_c}{\omega}, \tag{5}$$

where ω (radian/s) is the angular frequency of the "exploring wave" f (Hz), and ω_c(radian/s) is the angular collision frequency between electrons and heavier particles; ω_N is the angular plasma frequency with $\omega_N^2 = \frac{Ne^2}{\varepsilon_0 m}$ with electron density N ($1/m^3$), electron charge e ($1.6 \cdot 10^{-19}$ C), permittivity of free space ε_o($8.8542 \cdot 10^{-12}$ F/m), and electron mass m ($9.1095 \cdot 10^{-31}$ kg); ω_H is the angular gyrofrequency and $\omega_H = \frac{B_o|e|}{m}$ (radian/s) with the electromagnetic field strength B_o(Wb/m^2); ω_L is the longitudinal angular gyrofrequency and $\omega_L = \frac{B_o|e|}{m}\cos\Theta$ (radian/s); ω_T is the transverse angular gyrofrequency and $\omega_T = \frac{B_o|e|}{m}\sin\Theta$(radian/s).

When collisions are negligible (i.e., $Z \approx 0$),

$$n^2 \cong \mu^2 = 1 - \frac{2X(1-X)}{2(1-X) - Y_T^2 \pm \left[Y_T^4 + 4(1-X)^2 Y_L^2\right]^{1/2}}, \tag{6}$$

then according to the magnetoionic theory, a plane-polarized electromagnetic wave will be split into two characteristic waves: an ordinary wave which approximates the behavior of a wave propagating without an imposed magnetic field displayed with a sign "+" in Equation 6, and the wave with the sign "−" is called extraordinary wave.

The *Appleton-Hartree formula* assumes that the electron collision frequency ν is not dependent on the electron velocity. In the lower D and E regions of the ionosphere where the collision frequency ν is comparable with the wave frequency ω, this assumption no longer holds. To take this effect into account it is necessary to generalize the magnetoionic theory. Now, let us go back to Equation 1, and for the sake of simplicity, we set the magnetic field strength components $Y_T = Y_L = 0$, so that

$$n^2 \cong 1 - \frac{X}{1-iZ} = 1 - \frac{X}{1+Z^2} - \frac{iXZ}{1+Z^2}. \tag{7}$$

In Equation 7, after considering the real part of the refractive index only, using the binomial expansion for refractive index n, and then integrating it along the line of sight of the radio signal, we get for the ionospheric delay

$$d_{ion} \cong 40.3 \cdot \frac{TEC}{f^2 + \nu^2}, \tag{8}$$

where ν is the collision frequency (Hz). Equation 8 is very similar to Equation 7 with the difference of the inclusion of the term ν^2. The collision frequency ν becomes comparable with the microwave frequencies in the D layer where it can be as high as 10^9 (Hz) (Komjathy, 1997). Above the D layer, ν has a value about 10^4 (Hz). Using the largest D layer electron density at the high solar activity time ($1.3 \cdot 10^9$ (m^{-3})) (Bilitza, 1990) and assuming that the D layer ranges from 50 up to about 90 km, it turns out that by neglecting the collision frequency, in a worst case, we are introducing an error into the ionospheric delay using microwave frequencies at the 0.05 mm level. It is interesting to point out that the inclusion of the collision frequency ν actually reduces the refracting properties of the medium.

From Equation 7, we can now define the vertical incidence reflection which takes place when $n = 0$, that is,

$$1 - \left(\frac{f_N^2}{f^2}\right) = 0, \tag{9}$$

where f_N (Hz) is the plasma frequency at which a slab of neutral plasma with density N naturally oscillates after the electrons have been displaced from the ions and are allowed to move freely. f_N can also be expressed as

$$f_N^2 = \frac{Ne^2}{4\pi^2\varepsilon_0 m}, \tag{10}$$

where the individual parameters are described earlier in this section. For earth's ionosphere with e.g., N = 10^{12} (m^{-3}), a typical value for f_N is about 8.9 MHz (Bassiri and Hajj, 1993). The condition for a wave to be reflected at vertical incidence is $f = f_N$ which is the physical principle that will make it possible to use the techniques introduced in the following sections for ionospheric studies in *geodesy* and remote sensing.

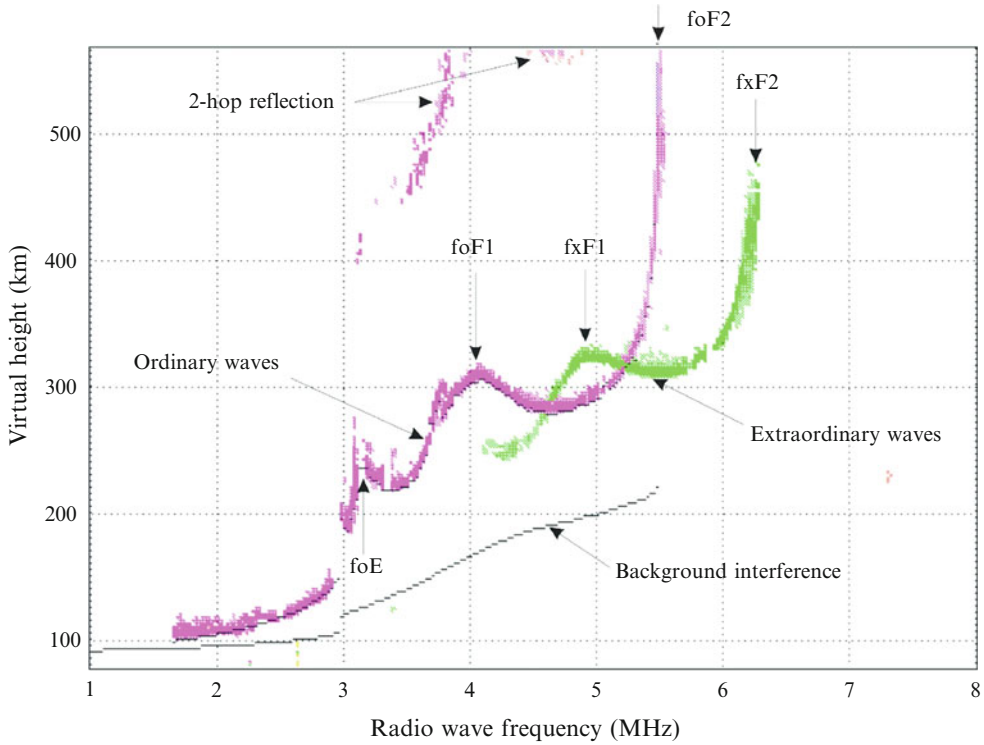

Ionospheric Effects on the Propagation of Electromagnetic Waves, Figure 2 Sample ionosonde data.

Ground-based techniques for ionospheric remote sensing

In section "Introduction to Ionospheric Propagation," we introduced the concepts of the *refractive index* for the *magnetoionic medium, plasma frequency*, and the *electromagnetic wave* refracting at vertical incidence (see Equation 9). Based on these principles, we will now discuss a few examples for ground- and space-based techniques as primary ionospheric remote sensing tools to measure critical ionospheric parameters and integrated electron densities (i.e., total electron content or TEC).

Ionosonde

Ionosondes function by emitting high frequency radio waves, sweeping from lower frequency to the higher, to measure the time required for the signal to travel and return from the refracting ionospheric layer. The radio-frequency pulse travels more slowly (group velocity) in the ionosphere than in free space; therefore, the virtual height is recorded instead of the true height. For frequencies approaching the maximum plasma frequency in a particular layer, the virtual height tends to become infinity because the wave has to travel a finite distance at effectively zero speed. Ionograms can provide the relationship between the radio wave frequency and virtual height of the reflecting ionospheric layer. From the ionograms, the characteristic values of virtual heights h_vE, h_vF1, and h_vF2 and critical (penetration) frequencies *foE*, *foF*1, and *foF*2 can be scaled manually or digitally. Modern ionosondes (digisondes) routinely scale ionograms. We present a sample ionogram in Figure 2 provided by MIT's Haystack Observatory. The data was observed with the Millstone Hill Digisonde. The radio wave frequency is plotted against the virtual height of the reflecting layer. We can clearly see that the virtual height steadily increases with the frequency up to the critical (penetration) frequency. In Figure 2, the critical frequencies *foE*, *foF*1, and *foF*2 can be obtained by taking a frequency reading when the virtual height has a local minimum (*foE*, *foF*1) or when it tends to approach infinity (*foF*2). In the figure, we can identify two curves representing the ordinary and extraordinary waves. The curves with the higher critical frequencies *fxF*1 and *fxF*2 are the extraordinary waves. The ordinary and extraordinary waves can be derived by using Equation 6 and then using $n = 0$ as a criterion for reflection at an ionospheric layer. After solving the equation, we will get separate solutions for the ordinary and the extraordinary waves. We can also identify a curve at the bottom of the plot which can be

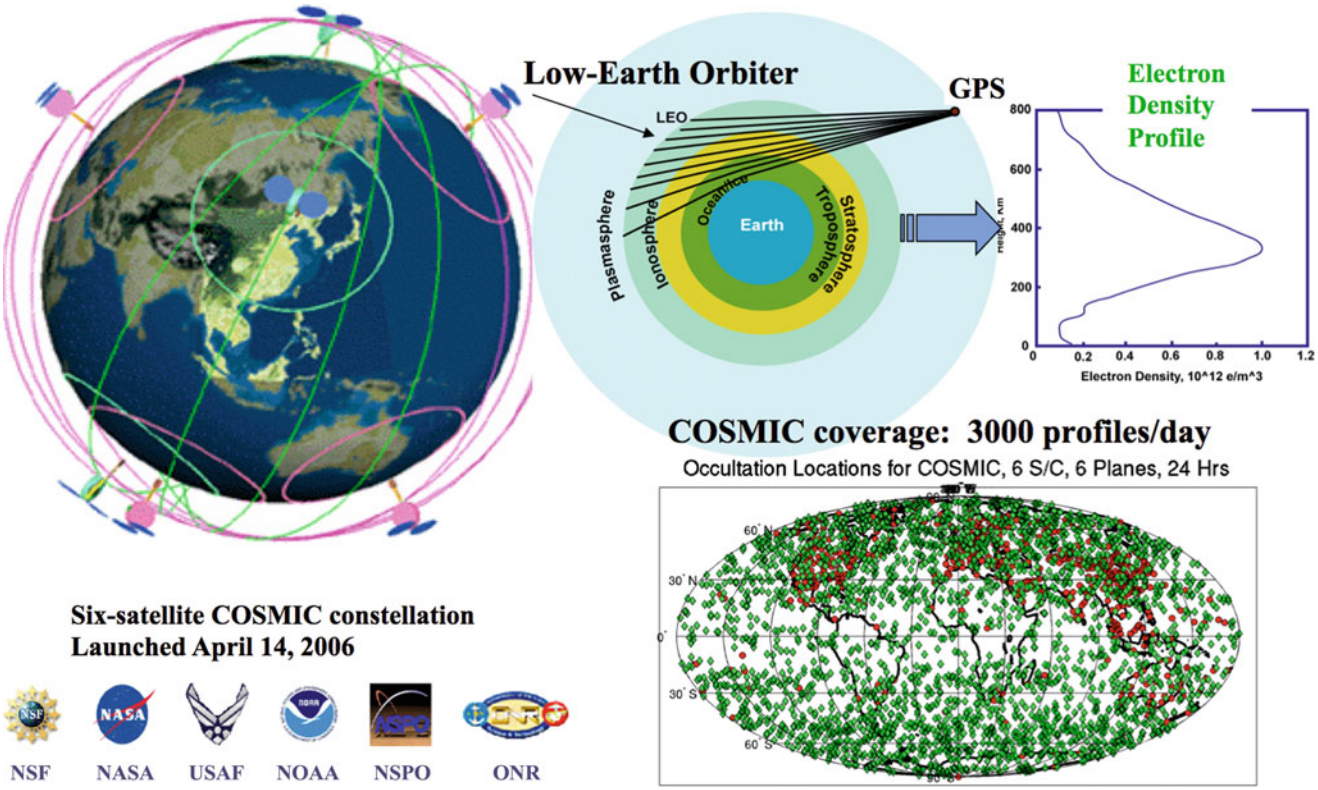

Ionospheric Effects on the Propagation of Electromagnetic Waves, Figure 3 Illustration for the COSMIC concept and constellation.

attributed to background interference. The so-called 2-hop reflection is due to the twice-reflected waves from the ionospheric layers with an intermediate ground reflection (Davies, 1990).

Incoherent backscatter radar

The incoherent scatter radar is the most powerful ground-based technique for the study of the earth's ionosphere and the interactions with the upper atmosphere, magnetosphere, and the interplanetary medium (see "*Radars*"). The technique is based on the radar principle which is the technique for detecting and studying remote targets by transmitting a radio wave in the direction of a target and observing the reflection of the wave. The target of any incoherent scatter radar is the electrons comprising the ionosphere. Since the amount of energy scattered by each electron is well known, the strength of the echo received from the ionosphere measures the number of electrons in the scattering volume and thus the electron density. The width of the spectrum is a measure of temperature of the ionosphere which can be different for ions and electrons. The shape of the spectrum is a sensitive function of the ratio of the electron and ion temperatures. Since the mixture of ions and electrons (also known as plasma) is constantly in motion in addition to the thermal motion, an overall shift of the spectrum can be detected from which the speed of the ions and electrons can be inferred (Komjathy, 1997).

Space-based remote sensing

We seem to be in the midst of a revolution in ionospheric remote sensing driven by the abundance of ground and space-based GPS receivers, new UV remote sensing satellites, and the advent of data assimilation techniques for space weather. The success of GPS/MET inspired a number of other radio occultation missions (see "*GPS, Occultation Systems*") to provide ionospheric measurements over oceanic regions, including the Argentine Satelite de Aplicaciones Cientificas-C (SAC-C), the US-funded Ionospheric Occultation Experiment (IOX), and Germany's Challenging Minisatellite Payload (CHAMP) (Jakowski et al., 2007). The joint US/Taiwan Constellation Observing System for Meteorology, Ionosphere, and Climate (COSMIC; http://cosmicio.cosmic.ucar.edu/cdaac/index.html), a new constellation of six satellites (see "*Observational Systems, Satellite*"), nominally provides up to 3,000 ionospheric occultations per day (Figure 3). The COSMIC 6-satellite constellation was launched in April 2006. COSMIC now provides an unprecedented global coverage of GPS occultation measurements (between 1,400 and 2,300 good soundings per day as of March 2009, see "*Limb Sounding,*

Atmospheric"), each of which yields electron density information with ~1 km vertical resolution. Calibrated measurements of ionospheric delay (total electron content) suitable for input into assimilation models are currently made available in near real time (NRT) from the COSMIC with a latency of 30–120 min. Similarly, NRT TEC data are available from two worldwide NRT networks of ground GPS receivers (~75 5 min sites and ~125 hourly sites, operated by JPL and others). The combined ground and space-based GPS datasets provide a new opportunity to more accurately specify the three-dimensional ionospheric density with a time lag of only 15–120 min. With the addition of the vertically resolved occultation data, the retrieved profile shapes are expected to model the hour-to-hour ionospheric "weather" much more accurately. JPL has begun integrating COSMIC-derived TEC measurements with ground-based GPS TEC data and assimilating these data into models such as JPL/USC Global Assimilative Ionospheric Model (GAIM) (originally sponsored by the US Department of Defense) so that three-dimensional global electron density structures and ionospheric drivers can be estimated.

The arrival of global, continuous datasets from diverse sources such as over 1,200 GPS receivers across the globe, satellite–satellite crosslink occultations, digisonde profiles, in situ satellite density measurements, and ultraviolet (UV) airglow measurements from low-Earth orbiters fueled the need to create models which are entirely data driven such as the persistence-driven thin shell model GIM (e.g., Mannucci et al., 1998; Komjathy et al., 2005) and various tomographic models such as MIDAS (Dear and Mitchell, 2006), EDAM (Angling and Cannon, 2004), and others (e.g., Rius et al., 1997). Further approaches, such as IDA3D (Bust and Crowley, 2007; Bust and Mitchell, 2008), attempt to incorporate data and ionospheric physics by use of models to define the a priori state of the ionosphere. In spite of high success in regions with excellent data coverage, these techniques are limited in forecasting ability. Newly emerged assimilative models involve first-principle physical models and yet also take in data, like the tomographic models, in an attempt to merge the benefits of both techniques. JPL/USC GAIM (e.g., Pi et al., 2003, 2004; Hajj et al., 2004; Wang et al., 2004; Mandrake et al., 2005), USU GAIM (e.g., Schunk, 2002; Scherliess et al., 2006), and the Fusion Numeric's assimilation model (e.g., Khattatov et al., 2004; Angling and Khattatov, 2006) have all been developed to address this need with significant variations in the forward modeling and data assimilation approaches to better characterize ionospheric specifications.

Conclusion

The advent of real-time global ground- and space-based measurements is expected to revolutionize the accuracy of ionospheric propagation specification, nowcast, and forecast. Recently, the NOAA Space Weather Prediction Center developed a new data assimilation product (Fuller-Rowell, 2005) that characterizes ionospheric TEC over the United States. In the next years, the real-time characterization of the global ionosphere is expected to become a standard product. This characterization will rely heavily on data from GPS measurements, but it will be enhanced by the real-time measurements from other sensors such as ionosondes or incoherent backscatter radars. As technology advances, societies of tomorrow are expected only to increase their need for highly accurate communications and navigation systems. Through collecting new data and finding new ways of analyzing ground and space-based GPS data to minimize signal propagation errors, scientists and operators will be sure to meet these future needs.

Acknowledgment

This research was carried out at the Jet Propulsion Laboratory, California Institute of Technology, under a contract with the NASA.

Bibliography

Angling, M. J., and Cannon, P. S., 2004. Assimilation of radio occultation measurements into background ionospheric models. *Radio Science*, **39**, RS1S08, doi:10.1029/2002RS002819.

Angling, M. J., and Khattatov, B., 2006. Comparative study of two assimilative models of the ionosphere. *Radio Science*, **41**, RS5S20, doi:10.1029/2005RS003372.

Bassiri, S., and Hajj, G. A., 1993. Higher-order ionospheric effects on the global positioning system observables and means of modeling them. *Manuscripta Geodaetica*, **18**, 280–289.

Bilitza, D. (ed.), 1990. *International Reference Ionosphere 1990*. Lanham, MD: National Space Science Data Center/World Data Center A for Rockets and Satellites. Report number NSSDC/WDC-A-R&S 90–22.

Bust, G. S., and Crowley, G., 2007. Tracking of polar cap ionospheric patches using data assimilation. *Journal of Geophysical Research*, **112**, A05307, doi:10.1029/2005JA011597.

Bust, G. S., and Mitchell, C. N., 2008. History, current state, and future directions of ionospheric imaging. *Reviews of Geophysics*, **46**, RG1003, doi:10.1029/2006RG000212.

Davies, K., 1966. *Ionospheric Radio Propagation*. New York: Dover.

Davies, K., 1990. *Ionospheric Radio*. London: Peregrinus.

Dear, R. M., and Mitchell, C. N., 2006. Ionospheric imaging at mid-latitudes using both GPS and ionosondes. *Journal of Atmospheric and Solar-Terrestrial Physics*, **69**(2007), 817–825.

Fuller-Rowell, T., 2005. USTEC: a new product from the Space Environment Center characterizing the ionospheric total electron content. *GPS Solutions*, **9**(3), 236–239.

Hajj, G. A., Wilson, B. D., Wang, C., Pi, X., and Rosen, I. G., 2004. Data assimilation of ground GPS total electron content into a physics-based ionospheric model by use of the Kalman filter. *Radio Science*, **39**, RS1S05, doi:10.1029/2002RS002859.

Hall, M. P. M., and Barclay, L. W., 1989. *Radiowave Propagation*. London: Peter Peregrinus.

Hunsucker, R. D., 1991. *Radio Techniques for Probing the Ionosphere*. New York: Springer.

Jakowski, N., Wilken, V., and Mayer, C., 2007. Space weather monitoring by GPS measurements on board CHAMP. *Space Weather*, **5**, S08006, doi:10.1029/2006SW000271.

Khattatov, B., Murphy, M., Cruikshank, B., and Fuller-Rowell, T., (2004). Ionospheric corrections from a prototype operational

assimilation and forecast system. In *Proceedings of IEEE Position, Location, and Navigation Symposium (PLANS)*. New York: Institute of Electrical and Electronic Engineers, pp. 518–526. Development of a physics-based reduced state Kalman filter for the ionosphere, *Radio Science*, **39**, RS1S04, doi:10.1029/2002RS002797.

Komjathy, A., 1997. *Global Ionospheric Total Electron Content Mapping Using the Global Positioning System*. Ph.D. dissertation, Department of Geodesy and Geomatics Engineering Technical Report No. 188, University of New Brunswick, Fredericton, New Brunswick, p. 248.

Komjathy, A., Sparks, L., Wilson, B., and Mannucci, A. J., 2005. Automated daily processing of more than 1000 ground-based GPS receivers to study intense ionospheric storms. *Radio Science*, **40**, RS6006, doi:10.1029/2005RS003279.

Langley, R. B., 1996. Propagation of the GPS signals. In *GPS for Geodesy*, International School, Delft, 26 March–1 April, 1995. Springer, New York.

Mandrake, L., Wilson, B., Wang, C., Hajj, G., Mannucci, A., and Pi, X., 2005. A performance evaluation of the operational Jet Propulsion Laboratory/University of Southern California Global Assimilation Ionospheric Model (JPL/USC GAIM). *Journal of Geophysical Research*, **110**, A12306, doi:10.1029/2005JA011170.

Mannucci, A., Wilson, B., Yuan, D., Ho, C., Lindqwister, U., and Runge, T., 1998. A global mapping technique for GPS-derived ionospheric total electron content measurements. *Radio Science*, **33**(3), 565–582.

Pi, X., Wang, C., Hajj, G. A., Rosen, G., Wilson, B. D., and Bailey, G. J., 2003. Estimation of ExB drift using a global assimilative ionospheric model: an observation system simulation experiment. *Journal of Geophysical Research*, **108**(A2), 1075, doi:10.1029/2001JA009235. Measurement, Jet Propulsion Laboratory, California Institute of Technology, Pasadena, CA, USA. (lukas.mandrake@jpl.nasa.gov) C. Wang, Department of Mathematics, University of Southern California.

Pi, X., Had, G. A., Wilson, B. D., Mannucci, A. J., Komjathy, A., Mandrake, L., Wang, C., and Rosen, I. G., 2004. 3-dimensional assimilative ionospheric modeling for regions of large TEC gradient, *Pmc* ION *NTM*, San Diego, January, 2004.

Rius, A., Ruffini, G., and Cucurull, L., 1997. Improving the vertical resolution of ionospheric tomography with GPS occultations. *Geophysical Research Letters*, **24**(18), 2291–2294.

Scherliess, L., Schunk, R. W., Sojka, J. J., Thompson, D. C., and Zhu, L., 2006. Utah state university global assimilation of ionospheric measurements Gauss-Markov Kalman filter model of the ionosphere:model description and validation. *Journal of Geophysical Research*, **111**, A11315, doi:10.1029/2006JA011712.

Schunk, R. W., 2002. *Global Assimilation of Ionospheric Measurements (GAIM)*. Paper presented at ionospheric effects symposium, Office of Naval Res., Alexandria, VA.

Schunk, R. W., and Nagy, A. F. (eds.), 2000. *Ionospheres: Physics, Plasma Physics, and Chemistry.* New York: Cambridge University Press, p. 333.

Wang, C., Hajj, G., Pi, X., Rosen, I. G., and Wilson, B., 2004. Development of the global assimilative ionospheric model. *Radio Science*, **39**, RS1S06, doi:10.1029/2002RS002854.

Cross-references

Electromagnetic Theory and Wave Propagation
Geodesy
GPS, Occultation Systems
Limb Sounding, Atmospheric
Magnetic Field
Radars

IRRIGATION MANAGEMENT

Steven R. Evett[1], Paul D. Colaizzi[1], Susan A. O'Shaughnessy[1], Douglas J. Hunsaker[2] and Robert G. Evans[3]
[1]USDA-ARS Conservation and Production Research Laboratory, Bushland, TX, USA
[2]USDA-ARS, Maricopa, AZ, USA
[3]USDA-ARS, Sidney, MT, USA

Synonyms

Irrigation automation; Irrigation scheduling; Precision irrigation; Site-specific irrigation

Definition

Irrigation management. The decision process and action of applying a chosen depth of irrigation water using a chosen application method at a chosen time to achieve defined agronomic and economic objectives.

Supervisory control and data acquisition (SCADA) system. An electronic hardware and software system that acquires data from sensors and controls the operations of other hardware in a supervisory fashion.

Irrigation automation. The use of in situ, remotely sensed, or near-surface remotely sensed crop, soil, and micrometeorological properties sensed by a supervisory control and data acquisition system as inputs to a decision-making algorithm in the system, which then applies defined amounts of water at defined times automatically through control of an integrated irrigation application system.

Introduction

Irrigation has been practiced around the world for thousands of years. Irrigation works greater than 6,000 years old have been found in regions as diverse as Southeast Asia, the Indian subcontinent, Central Asia, the Middle East, Egypt, and North and South America. Some of these systems simply diverted water during floods and allowed it to spread on otherwise unflooded valley lands. Others were more sophisticated and allowed diversion of water from permanent stream flow so that irrigation could occur more or less on demand. Although irrigation management occurs anytime that irrigation occurs, only in the latter systems did management include the aspects of application timing and amount. Early irrigation management involved two methods of sensing irrigation needs, either probing of the soil or observation of plant characteristics such as wilting or folding leaves and leaf color. Unfortunately, changes in plant characteristics observable by the human eye tend to occur only after there has been some loss of potential yield. As irrigation methods grew more sophisticated, so did the means of deciding when and how much water to apply. Tubular probes for extracting deep soil

USDA is an equal opportunity provider and employer.
Robert G. Evans has retired.

cores allow the soil water content below the surface to be examined, and the "feel and appearance" method of judging soil water content was regularized through studies that established the relationships between the feel and appearance of a handful of soil and its particle size distribution and water potential energy. Practical instrumentation for soil water sensing for irrigation management became widespread after the introduction of the neutron moisture meter (NMM) in the 1950s, but it was not until the 1980s that automated soil water sensors based on electromagnetic (EM) physics became available and not until the 1990s that they became widely available. In the meantime, irrigation management based on electronic sensing of plant condition remained largely in the realm of scientific studies.

After the publication of Penman's (1948) seminal paper, which established a theoretical basis for estimating plant water use (transpiration) from measurements of wind speed, solar radiation, air temperature, and humidity, a third and less direct paradigm for irrigation management was born. The new concept was based on the observation that crop water use varied with crop development (increasing with leaf area expansion) and with the evaporative demand, which could be estimated using Penman's equation. Later, Jensen (1968) defined a crop coefficient, K_c, as the ratio of actual crop water use ET_c to a potential or reference water use, ET_o:

$$K_c = ET_c/ET_o \quad (1)$$

The variation of K_c with crop growth (and leaf area index) was empirically determined as a function of days after planting or, more recently, growing degree days (GDD), the latter providing somewhat more stable relationships for K_c(GDD). Knowing the function K_c(GDD) for a crop and region and possessing local weather data, local crop water use, ET, can be estimated as:

$$ET = K_c ET_o \quad (2)$$

This paradigm has become the dominant one in state and federal efforts to provide irrigation scheduling information to farmers in the USA as evidenced by networks of weather stations and corresponding water use prediction systems established by both federal agencies (e.g., the AgriMET program sponsored by the Bureau of Reclamation in the Pacific Northwest) and states (e.g., CIMIS in California, AZMET in Arizona, the TXHPET Network in Texas, and the Oklahoma MESONET). The best of these provide decision support to some degree. For example, for each major crop in the region, the TXHPET Network provides crop water use values for the last day, 3 and 7 days for the closest weather station, and usually for each of three or four planting dates that span the earliest and latest planting in the current season. For crops such as corn that have short-season and long-season varieties, separate sets of values are provided for each. This reduces the management time needed to make irrigation decisions to a simple calculation of water already applied plus precipitation versus the crop water use. However, adoption by producers faces several obstacles, including lack of site specificity of weather stations, a need for corresponding in-field precipitation measurements, and an inability to characterize in-field variations in crop water use and water need. This is despite numerous and long-term efforts to improve the estimation of ET_o and K_c(GDD) by improving the theoretical underpinnings, taking into account plant cover effects and evaporation from soil more explicitly, and by improving siting and operation of weather stations (e.g., Monteith, 1965; Jensen et al., 1990; Allen et al., 1998; ASCE, 2005).

Given the current state of practice in irrigation management, the challenge for remote sensing is to provide irrigation management tools that allow producers to obtain comparable yield, yield quality, and water and nutrient use efficiencies profitably and sustainably, which means that such tools must be practical and cost-effective.

Spatial and temporal variability

Although traditional soil water, plant-based, and weather-based methods of irrigation scheduling address temporal variability of crop water need reasonably to very well, spatial variability is poorly addressed by these methods. Aerial and satellite imagery allow determination of spatial variability but often with temporal and spatial resolutions that are inadequate for day-to-day irrigation management (Jackson, 1984; Moran, 1994; Moran et al., 1997). The conjunctive use of coarse resolution thermal images with high-resolution images in the near-infrared and visible spectrums may provide solutions to the spatial resolution problem, but this is the subject of ongoing research (Kustas et al., 2004). These efforts are combined with those to merge data from satellites that return daily images with data useful for irrigation scheduling that are obtained only weekly or biweekly (Anderson et al., 2007). Such data fusion efforts were reviewed by Ha et al. (2013a, b). A key problem is that thermal infrared radiance data are the most useful for estimating crop ET, but these data are not available at high-enough temporal or spatial resolution and may even be lacking in new satellite platforms currently under development. The challenges that the status quo presents are being met by an array of near-surface remote sensing efforts, many of them using sensors that are mounted on moving irrigation systems (Evans and Sadler, 2008; Sadler et al., 2007) or on masts set in fields and some using aircraft platforms, including unmanned aerial vehicles (UAVs).

Remote sensing for irrigation management

Satellite and aerial remote sensing have became widespread only since the 1970s, although early efforts go back to the aerial photography from balloon platforms in the 1800s. As discussed elsewhere in this volume, the development of infrared film and electronic imaging in the visible spectrum and the invisible infrared and ultraviolet

spectrums allowed a new science of remote sensing of plant and soil condition to develop.

There are several approaches to irrigation management using remote sensing, including:

1. Scheduling irrigation to replace ET estimated from a reference ET (ET_o), calculated from local weather data, which is multiplied by a crop coefficient estimated with a crop coefficient function, K_c(NDVI), where NDVI is the normalized difference vegetative index (NDVI) or a similar index adjusted for reflectance from soil. The NDVI is based on canopy irradiance in the red and near-infrared bands, which can be remotely sensed.
2. Scheduling irrigations at a fixed amount of water whenever a trigger to irrigate is generated by the crop water stress index (CWSI), which is estimated using remotely sensed T_s and local weather data.
3. Scheduling irrigations at a fixed amount when triggered by the time-temperature threshold index (TTTI) reaching a crop and region-specific value. The TTTI is calculated using T_s.
4. Scheduling irrigation to replace ET estimated with the field surface energy balance (FSEB), which uses remotely sensed surface temperature, T_s, determined from thermal infrared data, and data on canopy cover and surface emissivity inferred from the near-infrared (NIR) and visible bands.
5. Sensing of crop characteristics in order to guide timing, placement, and amount of fertilizer and water through irrigation (or fertigation) systems of various orders of precision. The characteristics, including crop cover fraction, nitrogen status of leaves, disease, and pest damage, all of which vary spatially and temporally, are inferred from various remotely sensed vegetative indices (VIs).

Of the five approaches listed, only the CWSI and the TTTI have been commercialized and used by irrigators, the latter recently under the name BIOTIC (The mention of trade names of commercial products in this entry is solely for the purpose of providing specific information and does not imply recommendation or endorsement by the US Department of Agriculture.) (Upchurch et al., 1996) and the former since the 1980s. Practical use of both is quite limited currently. All of these approaches are the subjects of ongoing research efforts.

The ability to create broadband (thermal infrared to ultraviolet) images and to filter them into sub-band images led to breakthroughs in plant condition and cover sensing. Multispectral vegetation indices (VIs), such as the NDVI, are derived as ratios of signal strength in particular bands. Multispectral VIs have been widely researched as means to quantify various biophysical aspects of vegetation canopies, such as leaf area index (Moran et al., 1995), crop yield (Plant et al., 2000), and percent crop cover (Heilman et al., 1982). Thus, remote sensing of VIs provides a way to synoptically and instantaneously view crop conditions.

An approach that may improve the spatial representation of crop ET_c estimation is to incorporate remote sensing observations into irrigation scheduling protocols. A promising technique, introduced in the 1980s (Bausch and Neale, 1987), utilizes multispectral VIs to estimate corn crop coefficients. More recent research has shown that observations of multispectral VIs can provide real-time surrogates of crop coefficients for a variety of crops (Bausch, 1995; Neale et al., 2003; Hunsaker et al., 2005). Moreover, the use of remote sensing to infer the spatial distribution of K_c across the landscape can improve the ability of standard weather-based ET methods to more accurately estimate the spatial crop water use within an irrigated-field (Hunsaker et al., 2007) or at the farm-scale level (Johnson and Scholasch, 2005). The VI-based crop coefficient approach has strong practical appeal due to the longstanding familiarity and widespread use of crop coefficient methods and their relative operational simplicity. Also, this approach avoids some of the pitfalls with thermal bands, namely, the coarser spatial resolution and possible exclusion from future satellites. Nevertheless, implementation of the approach could be hindered by its reliance on empirical relationships between VIs and crop coefficients, by problems associated with the transferability of crop coefficient calibrations from one region to the next, and by timeliness and cost-effectiveness of the necessary imagery (Gowda et al., 2008).

Many methods of sensing plant water stress have been developed and studied, but only a few have impacted irrigation management. Dendrometers and leaf thickness and fruit size sensors have been used, mostly for high-value fruit and nut crops, but these approaches do not lend themselves to remote sensing. One of the earliest plant-based efforts that used near-surface remote sensing and that impacted irrigation management was the crop water stress index (CWSI) developed at the US Water Conservation Laboratory in the 1970s and 1980s (Idso et al., 1977, 1981; Jackson et al., 1981). The CWSI uses crop canopy temperature, typically sensed by an infrared thermometer, along with measured air temperature, humidity, wind speed, and solar radiation. The canopy-air temperature difference ($T_c - T_a$) is normalized to lower and upper limits of canopy-air temperature differences, which represent non-water-stressed and completely water-stressed crops, respectively. The CWSI is defined as

$$\mathrm{CWSI} = \frac{(T_c - T_a)_m - (T_c - T_a)_l}{(T_c - T_a)_u - (T_c - T_a)_l} \quad (3)$$

where the subscript "m" denotes measured, "l" denotes a lower baseline (non-water-stressed crop), and "u" denotes an upper limit (completely water-stressed crop). The $(T_c - T_a)_l$ and $(T_c - T_a)_u$ limits may be estimated on an empirical (Idso et al., 1981) or theoretical (Jackson et al., 1981) basis. Both approaches require, at minimum, measurements of air temperature and humidity. The latter approach also requires wind speed, solar radiation, and

estimates of bulk canopy resistances. Meteorological parameters were not widely available until automated agricultural weather stations began to appear during the early 1980s (Howell et al., 1984). Furthermore, it was not until this time that basic data on bulk canopy resistances became established for a wide variety of crops and local conditions. Hence, the empirical CWSI received greater attention than its theoretical counterpart early on.

As initially developed in research and deployed for irrigation management, the CWSI employed a handheld infrared thermometer used to measure canopy temperatures at one time of day near solar noon. Although theoretically enticing, the CWSI has not been widely used for irrigation management due to various problems, including lack of a stable signal during cloudy periods, difficulty in determining the lower baseline and upper limit and nonuniqueness of these limits, and problems with measuring a meaningful canopy temperature that is representative of the field crop when soil background is visible, which might occur during part or all of the irrigation season. Moran et al. (1994) extended the CWSI concept where the upper and lower limits were defined as mixtures of soil and vegetation temperatures and termed this the water deficit index (WDI). However, both the CWSI and WDI may be sensitive to small errors in the upper and lower temperature limits, which often results in values outside the theoretical range from zero to one. The effect of sunlit vs. shaded soil and a well-watered crop underlain by dry soil (e.g., subsurface drip irrigated soil, Colaizzi et al., 2003) may further confound errors in estimating these limits.

Although the early work with the CWSI was done using handheld infrared thermometers to sense the thermal infrared radiation from crop canopies, later work has shown that maps of the CWSI or WDI can be created from aerial and satellite images or images compiled from ground-based sensors aboard self-propelled irrigation systems (Colaizzi et al., 2003; Peters and Evett, 2008; O'Shaughnessy et al., 2008). For example, an empirical CWSI (eCWSI) was determined to be a robust stress index for irrigated vineyards:

$$\text{eCWSI} = \frac{T_c - T_\text{w}}{T_\text{dry} - T_\text{w}} \tag{4}$$

where T_c was the temperature (°C) of the center of the crop canopy computed from aerial thermal images, T_w was the temperature from an artificial wet surface that acted as a substitute for the well-watered baseline temperature, and T_dry was estimated by adding 5 °C to the maximum dry bulb temperature recorded for the specific field day (Jones, 1992; Möller et al., 2007). Similar relationships were shown for cotton grown in the Texas High Plains where calculated eCWSI values were compared to stem leaf water potential (Ψ_L) and in the South of Israel where comparisons were made with Ψ_L and stomatal conductance (Evett and Alchanatis, 2007). These empirical relationships were more robust than the theoretical model of Jackson et al. (1981) relating crop canopy temperatures to crop water status, and they provided a basis for spatial mapping of Ψ_L at the field scale. In areas where irrigation decisions are based on Ψ_L, this modeling may replace the labor-intensive efforts of Ψ_L measurements.

Although fundamentally related to plant water status, the CWSI faces a number of problems that have so far prevented its widespread use. The well-watered baseline is a function of plant species and for a single species can vary by important amounts between varieties (e.g., cotton: Hatfield et al., 1987). Empirical determinations of lower baseline vary depending on how "well-watered" is defined. For partial canopies, emittance from soil can bias the measure of T_c, a problem for all methods that use T_c. Also, viewing angle of the infrared sensor will affect the temperature reading, as will flowering and seed filling in some crops (corn, sorghum, and wheat). Taking readings at an angle from nadir and taking readings from opposing viewpoints are techniques used to reduce these biases. However, these techniques are not easily achieved from satellite and aircraft platforms. For these reasons, the CWSI in its many forms has not been widely adopted for use in irrigation management.

The TTTI is the number of minutes in a day that a canopy is above a species-specific threshold canopy temperature. If the TTTI exceeds a threshold time (min), which is specific to a species and climatic region, then an irrigation is triggered. The threshold time was determined by finding the average number of minutes in a day throughout the irrigation season that the canopy of a well-watered crop was above the threshold temperature. The threshold temperature was originally conceived as the temperature at which photosynthetic assimilation peaks (Burke and Oliver, 1993). However, Evett et al. (1996, 2000, 2006a) showed that the threshold temperature could be varied as long as a corresponding threshold time was determined from canopy temperatures measured on a well-watered crop. The method suffers from the same viewing angle problems that affect the CWSI. And the threshold temperature may be variety specific, not just species specific. Also, the method requires a continuous record of canopy temperature throughout the daylight hours, something not readily achieved using airborne or satellite platforms. The latter problem was overcome by Peters and Evett (2004) who devised an algorithm to scale a one-time-of-day canopy temperature measurement so as to estimate a continuous course of canopy temperatures for daytime, except for 1 h after sunrise and 1 h before sunset, with sufficient accuracy to trigger irrigations using the TTTI (<1 °C error). This algorithm may have utility in scaling thermal image data from airborne or satellite platforms to produce maps of TTTI values and thus maps of crop water stress over large areas.

Thermal radiometric measurements of crop canopy temperature for automatic irrigation scheduling using the TTTI have been successful for drip-irrigated plots (Evett et al., 1996) and low-energy precision application (LEPA) irrigation using a center pivot sprinkler (Peters and

Evett, 2008). This simplified approach avoids the complexity of the CWSI by relying on the feedback effect of irrigation, which by providing water to plants allows increased transpiration and resultant cooling of the canopy. Wired thermal radiometers are now being replaced with wireless infrared thermometers and wireless sensor networks to establish remote links for data collection, communication, and control of irrigation systems (O'Shaughnessy and Evett, 2007). The specific implementation of the TTTI embodied in the BIOTIC patent has been licensed and commercialized since 2008. Although it is difficult to envision application of the TTTI using data from satellite or aircraft platforms, it is readily applied using near-surface remote sensing with sensors mounted on towers or moving irrigation system superstructures. In fact, use of moving irrigation systems as sensing platforms has allowed the implementation of field mapping of crop water stress levels and relative yield potential (Peters and Evett, 2007) as well as irrigation control.

The field surface energy balance (FSEB) has long been recognized for its promise in calculating the latent heat flux, LE, due to ET, from the other energy balance terms in

$$0 = \mathrm{LE} + G + H + R_\mathrm{n} \tag{5}$$

where G is soil heat flux, H is sensible heat flux, and R_n is net radiation (all fluxes taken positive toward the surface, often in W m^{-2}). In field research, many or all of these fluxes are measured, but from a remote sensing perspective, the surface brightness in the thermal infrared (used to estimate T_s) and the brightness in the near-infrared and visible bands are used to estimate R_n and H. The value of G is taken as a fraction of R_n or some function of R_n and plant cover (estimated from a VI), and ET as a depth of water per unit time (m s^{-1}, positive toward the atmosphere) is evaluated as the residual

$$\mathrm{ET} = -\mathrm{LE}/(\lambda\rho_\mathrm{w}) = (R_\mathrm{n} + G + H)/(\lambda\rho_\mathrm{w}) \tag{6}$$

where $H = \rho_\mathrm{a} c_\mathrm{p}(T_\mathrm{s} - T_\mathrm{a})/r_\mathrm{a}$; T_s is assumed equal to the aerodynamic surface temperature, T_o (°C); r_a is aerodynamic resistance, which is calculated as a function of crop height, h_c, and wind speed, u_z (m s^{-1}), measured at an elevation z (m); c_p is the heat capacity of air (~1,003 kJ kg^{-1} K^{-1}); λ is the latent heat of vaporization ($\sim 2.45 \times 10^6$ J kg^{-1}); ρ_w is the density of water (~1,000 kg m^{-3}); and ρ_a is air density (kg m^{-3}, $\rho_\mathrm{a} \approx 1.291 - 0.00418 T_\mathrm{a}$). When R_n, G, T_s, T_a, h_c, and u_z are measured in the field, Equation 6 can estimate ET with fair accuracy (Kimball et al., 1999) for full-cover crop surfaces. Because energy balance models have more numerous applications besides cropped surfaces or irrigation management, they have been investigated more extensively compared with the VI-based crop coefficient approach.

Remote sensing approaches to FSEB evaluation for ET are numerous and include both single-surface approaches that assume that the crop can be modeled as a big leaf (i.e., Equation 6) (e.g., Bastiaanssen et al., 2005; Allen et al., 2007a, b) and two-surface approaches that evaluate the energy and water balances for both canopy and soil surfaces and thus must estimate the crop cover fraction (e.g., Evett and Lascano, 1993; Norman et al., 1995; Kustas and Norman, 1999; Colaizzi et al., 2012). While providing useful knowledge of regional ET and its spatial and temporal distribution, FSEB predictions that rely on satellite images are not used for irrigation management due to lack of daily data with sufficient resolution to match the field scales at which irrigation is managed (Gowda et al., 2008). Attempts to resolve this problem with existing satellite data involve using infrequent, higher-resolution data such as that from Landsat (90 m resolution in the thermal IR, 16 day repeat time) in combination with lower-resolution more frequent data such as that from MODIS (1,000 m resolution in the thermal IR, daily). Such a combination was demonstrated with the DisALEXI (disaggregated atmosphere land exchange inverse) model (Anderson et al., 2007; Kustas et al., 2007; Norman et al., 2003), but no testing of this approach for irrigation management has ensued. While aircraft platforms could resolve some of these problems, so far there has not been widespread use of aircraft platforms to provide imaging for irrigation management, probably due to cost.

The FSEB using remotely sensed data typically provides an instantaneous value of ET, which must be scaled to daily ET using various methods such as the evaporative fraction (which is assumed constant during daylight hours) or reference ET (which is also assumed constant relative to latent heat flux during daylight hours) (Colaizzi et al., 2006). Models of the FSEB that use remote sensing include the two-source model (TSM, Norman et al., 1995; Kustas and Norman, 1999), the surface energy balance algorithm for land (SEBAL, Bastiaanssen et al., 1998), and mapping ET with internalized calibration (METRIC, Allen et al., 2007a, b). Gowda et al. (2008) reviewed these and several other approaches and reported that daily ET estimation errors ranged from 3 % to 35 % but that almost all studies compared FSEB ET with ET sensed by Bowen ratio or eddy covariance methods, which themselves have large errors. Colaizzi et al. (2012) evaluated the two-source energy balance model of Norman et al. (1995) and Kustas and Norman (1999) where crop ET was measured with weighing lysimeters at Bushland, Texas, and radiometric temperature was measured with infrared thermometers that viewed the lysimeter surface. Crops included fully irrigated corn, alfalfa, soybean, and winter wheat; deficit-irrigated cotton; and dryland grain sorghum. This study differed from previous two-source energy balance model testing studies, which mainly used Bowen ratio or eddy covariance systems to indirectly estimate ET and used remotely sensed data from satellite or airborne platforms to run the models. The root mean squared errors between modeled and observed energy fluxes were slightly greater in the Colaizzi et al. (2012) study compared with the previous studies, which was probably related to the

methods used to estimate ET and radiometric surface temperature.

The vast majority of energy balance model testing studies have been at the watershed or regional scale and used satellite data, which are too coarse and/or infrequent for irrigation management. Moreover, ET estimates from regional models are often inaccurate due to problems with correctly estimating the surface radiation balance components (Berbery et al., 1999). However, several studies, using either ground-based or airborne sensor platforms to achieve suitable spatial scales (i.e., a few meters or less), have shown the utility of energy balance and stress index models for irrigation management (Colaizzi et al., 2003; French et al., 2007), including automatic irrigation scheduling and control (Evett et al., 1996, 2000, 2006a; Peters and Evett, 2008). One outcome of the years of research on remote sensing using satellite platforms has been the cross-fertilization of the irrigation engineering field where ground-based sensor platforms are more likely to be utilized but where the principles of remote sensing are just as applicable. Ground-based or near-surface remote sensing provides data of high temporal and spatial resolution that can be very useful in irrigation management, but largely without the need for correction for interference from the atmosphere. Remote sensing principles and techniques are routinely used, including spectral data acquisition and processing, VI relationships to plant cover and condition, thermal infrared data acquisition, relationships to plant condition, and energy balance.

In addition to the main avenues of research and application involving remote sensing for irrigation management, there are some areas that have not seen serious or successful efforts due to either intractable problems, newness of the approach, or lack of direct applicability. Several researchers have documented relationships between surface soil water content or soil profile water content and temperature indices. Sadler et al. (2000) found that the canopy-air temperature difference, $(T_c - T_a)$, explained 60 % of the variation of the fraction of available water in the top meter of soil. Colaizzi et al. (2003) developed relationships between the CWSI of flood-irrigated cotton on a sandy loam with a soil water stress index and with both the fractional soil water content depletion and depth of depletion. However, they stressed that the relationship was strongest for severely depleted soil and water-stressed plants and would lose relevance for frequently and more adequately irrigated crops. Passive and active microwave radiation and synthetic aperture radar have been used for surface water content estimation (top few centimeters of soil) but encounter the problems of imprecisely known sensing depth, interference from vegetation, and spatial resolution too coarse for irrigation management. Characterization of soil roughness needed to produce accurate soil water content estimates is not well understood, and only regional-scale mapping is possible (Verhoest et al., 2008). A series of field campaigns with various types of ground truthing have explored this and related approaches to soil water content sensing (Washita'92, Washita'94, SGP97, SGP99, SMEX02, SMEX03, SMEX04, SMEX05, CLASIC – Land, SMAPVEX08; e.g., Jackson et al., 1995, 1999, 2005, 2008; Jackson and Hsu, 2001). This approach is more useful for synoptic studies than for irrigation management (e.g., Zhan et al., 2008). Some recent work has focused on using thermal remote sensing surface temperature data as input to a FSEB model with a soil water component in order to drive estimates of profile water content (Crow et al., 2008). This is similar to attempts made using near-surface remote sensing of canopy temperatures to drive models of the soil-plant-atmosphere continuum. To date, these approaches have not been useful in field-scale irrigation management.

Current obstacles

Remotely sensed data must meet several criteria to be suitable for irrigation management, but present satellite and airborne platforms do not meet one or more of these requirements, which include spatial resolution, repeat frequency (i.e., temporal resolution), accuracy, and turnaround time. Jackson (1984) discussed these requirements and concluded that spatial resolution must be on the order of a few meters, repeat frequency no more than a few days (although hourly would be most desirable), and turnaround time (i.e., the interval from actual field measurements to the usable data product) no more than a few minutes. Since then, irrigated area under moving and drip irrigation systems has greatly increased (e.g., $>$80 % in the Southern Great Plains), and these systems require data at intervals not greater than a day. Present satellite platforms with thermal bands have a trade-off between spatial and temporal resolution. Although satellite data have been successfully used to construct spatially distributed ET maps at the watershed (Allen et al., 2007b) or continental scale (Kustas et al., 2004), they lack adequate spatial resolution for irrigation management and have turnaround times on the order of weeks or more due to extensive processing requirements (i.e., atmospheric and geometric correction). Sharpening algorithms, such as TsHARP, do not accurately recover information at subfield scales suitable for irrigation management (Agam et al., 2007, 2008). Airborne platforms can potentially meet both the spatial and temporal requirements but are cost prohibitive and also suffer from undue turnaround times because automated processing algorithms have yet to be developed. Moran (1994) demonstrated the shortcomings of both satellites and aircraft for irrigation management, which were mainly due to turnaround time, but also due to inexplicable lapses in data delivery from cooperating entities. More recently, there have been efforts to adopt unmanned air vehicles (UAVs) to carry sensors suitable for on-farm management applications (Herwitz et al., 2004; Xiang and Tian, 2007; Chao et al., 2008). Unresolved issues include the need to reduce sensor package mass, reliable radio control, lack of control

in windy conditions, orthogonal correction of non-nadir views, and geo-referencing.

Rigorous FSEB model assessment and testing is contingent on both accurate ground truth and remotely sensed data. High-quality ground truth data are particularly expensive and difficult to obtain, and the simultaneous acquisition of remotely sensed data is indeed challenging. These factors have impeded development of more robust models. Weighing lysimeters are the most direct and potentially accurate method of ET measurement (Howell et al., 1995); however, they are expensive, not portable, and require highly trained personnel to operate and maintain. ET may also be derived with good accuracy as the residual of the soil water balance if measurements of irrigation, rainfall, and soil water throughout the profile are available, and provided other sources and sinks that are difficult to measure can be minimized or eliminated (e.g., run-on, runoff, deep percolation, and upward capillary flux from a shallow water table). However, accurate measurement of the soil profile water content has been limited to destructive and labor-intensive gravimetric sampling or the neutron moisture meter (NMM), which is also labor intensive and cannot be operated unattended. Electromagnetic soil water sensors presently on the market, which are appealing in that they may be automated, suffer from very poor accuracy in most soils (Evett et al., 2006b, 2008, 2009; Mazahrih et al., 2008). Other techniques of estimating ET include Bowen ratio, eddy covariance, and meteorological flux towers. These systems are portable, relatively low cost, and easily automated, and hence have been the most popular ground truth techniques for model testing (validation) studies. However, the Bowen ratio method assumes that the conductivity for water vapor flux, K_v, equals the conductivity for heat flux, K_h, and is therefore subject to errors during advective conditions and can also be sensitive to fetch and instrument bias (Todd et al., 2000). Eddy covariance techniques sense turbulent fluxes across a field directly, but the energy balance is often not closed (Evett et al., 2012a; Twine et al., 2000) even when additional procedures or corrections are used. Meteorological flux towers have been used extensively in desert environments (Kustas and Norman, 1999), but their accuracies over cropped surfaces or in advective environments are presently not known. At present, the most accurate ground truth is from weighing lysimeters and soil water balance ET estimates made using the NMM. Unfortunately, most FSEB model validation efforts have not been able to use those methods. A recent example of using weighing lysimeter and soil water balance measures of ET is, however, available in a special issue of Advances in Water Resources (Evett et al., 2012b).

Ground-based sensors aboard farm machinery, such as self-propelled irrigation systems, are an alternative to satellite or airborne platforms. In regions where center pivot or lateral-move irrigation systems are popular, they appear to be a logical sensor platform for irrigation management, since they pass over the field at regular intervals. Ground-based sensors may greatly reduce turnaround time because they do not require extensive processing such as atmospheric or geometric correction. Phene et al. (1985) is an early example of deployment of infrared thermometers aboard a self-propelled irrigation system. However, thermal radiometric sensors are responsive to soil emittance and to reflection from vegetative canopy: Less than full canopy cover may cause false-positive irrigation triggers in the early growing season and thermal measurements from mixed pixels of sunlit soil and vegetation can provide unduly high temperature readings. Discrimination between thermal radiance from soil and vegetation in low cover or leaf area index situations is a problem still under active investigation, and solution will probably require imaginative combination of multispectral data, sensor view angles, and understanding of canopy and soil characteristics.

Center pivot and linear move irrigation systems generally apply water quite uniformly; however, substantial variations in soil properties and water availability exist across most fields. In these cases, the ability to manage site-specific irrigation to match spatially and temporally variable conditions can offer opportunities for increased application efficiencies, reduced environmental impacts, more effective agrichemical use, and the potential to improve crop yields and quality. In addition, these types of systems afford the opportunity to precisely manage deficit irrigation strategies. The development of in-field sensor-based control of site-specific applications of water and water-soluble nutrients through the irrigation system offers an effective means to implement site-specific technologies, but the seamless integration of sensors, irrigation control, data interface, software design, and communication at costs that are in balance with the profit advantages of site-specific applications is challenging.

Several researchers have investigated the potential use of a feedback from wireless in-field sensing systems to control variable-rate irrigation systems, but few have fully integrated these systems. An exception is the TTTI system implemented for automatic irrigation control of drip and center pivot irrigation (Evett et al., 2006a; Peters and Evett, 2008). Miranda et al. (2003) used a closed-loop irrigation system and determined irrigation amount based on distributed soil water measurements. Shock et al. (1999) used radio transmission for soil moisture data from data loggers to a central computer logging site. Wall and King (2004) explored designs for smart soil moisture sensors and sprinkler valve controllers to implement plug-and-play technology and proposed architectures of distributed sensor networks for site-specific irrigation automation (King et al., 2000). Kim et al. (2008, 2009) used distributed sensor networks and GPS with Bluetooth® wireless communications to control water applications with off-site computers. Software design for automated irrigation control has been studied by Abreu and Pereira (2002). They designed and simulated solid set sprinkler irrigation systems by using software that allowed the design of a simplified layout of the irrigation system.

The coordination of control with data from sensors is effectively managed using data networks and low-cost microcontrollers (Wall and King, 2004). A hardwired system from in-field sensing station to a base station requires extensive time and cost to install and maintain. It may not be feasible to get the system hard wired for long distances, and it may not be acceptable to growers because it can interfere with normal farming operations and the maintenance costs may be unacceptable. A wireless data communication system can provide dynamic mobility and cost-free relocation. Radio frequency technology has been widely adopted in consumer wireless communication products, and it provides numerous opportunities to use wireless signal communication in agricultural systems. Industrial wireless standards such as the ZigBee protocol are open standards that allow integration of sensors and equipment from different manufacturers into a supervisory control and data acquisition (SCADA) system (O'Shaughnessy and Evett, 2007, 2008). Present challenges include meeting power requirements of remote sensors, radio interference, cost reduction, interfacing with existing irrigation control equipment, and development of rugged and inexpensive but accurate sensors (e.g., reflectance photodiodes and infrared thermometers).

Importance of unified technologies

Inherent in the evolution of on-farm water management is the integration of irrigation, fertilizer, and pest management strategies into systems that optimize total management practices for temporal and spatial variability using precision agriculture tools. This integration will require broad systems approaches that physically and biologically optimize irrigations with respect to water delivery and application schemes, rainfall, critical growth stages, soil fertility, location, and weather. Spatial and temporal management strategies will need to address site-specific crop requirements for water, nutrition, pest management, and irrigation scheduling in both agrarian and urban settings.

Improved irrigation technologies, while usually requiring less field labor, often demand more intensive management. Thus, support aids must also be developed that improve the producer's ability to implement decisions quickly and easily; however, this also requires control and monitoring systems. Decision support systems are needed to help make timely decisions based on complex inputs. Climatic variations and pest outbreaks require precisely timed and placed water and chemical applications on a daily and seasonal basis. The decision support process must also provide accurate predictions of crop water use, application efficiencies, and uniformities to improve management flexibility.

The commercialization of irrigation automation is dependent on the development of economical and reliable wireless sensors and sensor networks. Communication modules for each sensor type and network must be interchangeable. The progress of precision irrigation depends on the seamless automatic operation of irrigation systems accomplished by the flexible integration of controllers and sensors, algorithms for data acquisition and control, compatible sensor hardware that is field installable and easy to maintain (plug-and-play format), and user-friendly interfaces that provide practical, robust, and timely decision-making support to the grower.

Conclusions

Ensuring the success of irrigated farming enterprises will require the development of reliable, timely information on field and plant status to support decision making. Remote sensing of plant and soil status using integrated satellite, aerial, and field-level plant and soil-based sensor systems can provide information on plant and soil nutrient and water status. Nevertheless, this technology needs further development to improve spatiotemporal modeling and hands-on use for on-farm management as well as irrigation district operations. Better systems and methods capable of measuring specific plant parameters (e.g., nutrient status, water status, disease, and competing weeds) on a timely basis are becoming available and are expected to provide information required to enhance use in crop modeling and improve within-season management.

Several remote sensing approaches have been shown to provide spatially distributed information on ET and plant water stress that is meaningful for irrigation management. These approaches use reflectance and thermal radiance measurements of the surface; those discussed herein included water stress indices, vegetation index (VI)-based crop coefficients, and surface energy balance models. Water stress indices are generally used to detect plant water stress and may be useful for appropriately timing irrigation events. The VI-based crop coefficient approach can be used to estimate crop ET when a reference ET value is available. This approach is essentially the same as the widely used crop coefficient-reference ET paradigm, where crop coefficients are based on calendar days or heat units, but VI-based crop coefficients estimated from images provide spatial information of actual crop conditions, unlike conventional crop coefficients. Surface energy balance models are generally classed as either single-layer or two-layer approaches, where the latter computes the energy fluxes of the soil and vegetation separately. Both types of energy balance models compute instantaneous latent heat flux, which can be converted and scaled to daily ET. The VI-based crop coefficient approach requires reflectance measurements but not thermal measurements as do water stress indices and energy balance models. However, the VI-crop coefficient approach is more empirically based and subject to local conditions, which may reduce geographic transferability. Energy balance models have been researched more extensively than VI-based crop coefficients, as they are applicable to other vegetated surfaces besides crops.

Routine application of remote sensing to irrigation management remains subject to several obstacles, which are generally related to model robustness and sensor platform cost, timeliness, and spatial resolution. The development of robust models has been hampered somewhat by inherent challenges in measuring ET or plant water stress for ground truth while simultaneously measuring surface reflectance and temperatures. The need for accurate and robust models is critical if they are to provide meaningful decision support for the rational allocation and timing of irrigation water. Just as critical is a fundamental understanding of model limitations, so that misapplication may be avoided. Sensor platforms, in order to be suitable for irrigation management, must provide data at spatial resolutions of a few meters, at least daily repeat frequencies, and have turnaround times of a few minutes. Existing satellite and airborne platforms do not meet one or more of these criteria. Key satellite platforms for thermal infrared data with sufficient spatial (but not temporal) resolution for irrigation management (LandSat 5 and 7) are nearing the end of their useful lives, and there is no near-term replacement, which makes expediting of the only new satellite planned with thermal IR capability (HyspIRI, with 45 m resolution and a 5 day cycle) essential (Anderson and Kustas, 2008). Unmanned air vehicles (UAVs) and ground-based sensors aboard self-propelled irrigation systems have the potential to avoid some of the pitfalls of satellite or airborne platforms but nonetheless have other technical and cost issues to be overcome. At a time when thermal infrared data from satellite remote sensing is finally being used for effective water resource management at large scales (Allen et al., 2008), and when the technology for managing irrigation at small scales is becoming well developed and would be applicable if resolution in time and space were improved, the USA should be highly motivated to, rather than end its efforts, become once again a leader in space-based platforms for thermal infrared imaging at high spatial and temporal resolution.

Irrigated agriculture will be expected to provide more crops for a growing world population with less water resources. Also, farm consolidation continues in many regions, resulting in greater area being managed by fewer personnel. The need for better irrigation management tools that reduce management time is apparent. Remote sensing, with its capabilities of spatially distributed information, is one technology that may fulfill this need. Therefore, research and development efforts should continue to emphasize model validation and refinement and more suitable platforms and sensors capable of delivering timely irrigation management guidance and control at scales small enough to affect within-field management.

Bibliography

Abreu, V. M., and Pereira, L. S., 2002. *Sprinkler Irrigation Systems Design Using ISAMim*. ASABE Paper No. 022254. St. Joseph: ASABE.

Agam, N., Kustas, W. P., Anderson, M. C., Li, F., and Colaizzi, P. D., 2007. Utility of thermal sharpening over Texas high plains irrigated agricultural fields. *Journal of Geophysical Research*, **112**, D19110, doi:10.1029/2007JD008407.

Agam, N., Kustas, W. P., Anderson, M. C., Li, F., and Colaizzi, P. D., 2008. Utility of thermal image sharpening for monitoring field-scale evapotranspiration over rainfed and irrigated agricultural regions. *Geophysical Research Letters*, **35**, L02402, doi: 10.1029/2007GL032195.

Allen, R. G., Periera, L. S., Raes, D., and Smith, M., 1998. *Crop Evapotranspiration: Guidelines for Computing Crop Water Requirements*. Rome: United Nations FAO. Irrig. and Drainage Paper No. 56.

Allen, R. G., Tasumi, M., and Trezza, R., 2007a. Satellite-based energy balance for mapping evapotranspiration with internalized calibration (METRIC)-model. *Journal of Irrigation and Drainage Engineering*, **133**(4), 380–394.

Allen, R. G., Tasumi, M., Morse, A., Trezza, R., Wright, J. L., Bastiaanssen, W., Krambler, W., Lorite, I., and Robinson, C. W., 2007b. Satellite-based energy balance for mapping evapotranspiration with internalized calibration (METRIC) – applications. *Journal of Irrigation and Drainage Engineering*, **133**(4), 395–406.

Allen, R. G., Toll, D., Kustas, W., and Kleissl, J., 2008. From high overhead: ET measurement via remote sensing. *Southwest Hydrology*, **7**(1), 30–32.

Anderson, M., and Kustas, W., 2008. Thermal remote sensing of drought and evapotranspiration. *EOS Transaction, American Geophysical Union*, **89**(26), 233–234.

Anderson, C. M., Kustas, W. P., and Norman, J. M., 2007. Upscaling flux observations from local to continental scales using thermal remote sensing. *Agronomy Journal*, **99**, 240–254.

ASCE, 2005. In Allen, R. G., Walter, I. A., Elliot, R. L., Howell, T. A., Itenfisu, D., Jensen, M. E., and Snyder, R. L. (eds.), *The ASCE Standardized Reference Evapotranspiration Equation*. Reston, VA: American Society of Civil Engineers.

Bastiaanssen, W. G. M., Menenti, M., Feddes, R. A., and Holtslang, A. A., 1998. A remote sensing surface energy balance algorithm for land (SEBAL): 1 formulation. *Journal of Hydrology*, **212–213**, 198–212.

Bastiaanssen, W. G. M., Noordman, E. J. M., Pelgrum, H., Davids, G., Thoreson, B. P., and Allen, R. G., 2005. SEBAL model with remotely sensed data to improve water-resources management under actual field conditions. *Journal of Irrigation and Drainage Engineering*, **131**(1), 85–93.

Bausch, W. C., 1995. Remote sensing of crop coefficients for improving the irrigation scheduling of corn. *Agricultural Water Management*, **27**(1), 55–68.

Bausch, W. C., and Neale, C. M. U., 1987. Crop coefficients derived from reflected canopy radiation: a concept. *Transactions of ASAE*, **30**(3), 703–709.

Berbery, E. H., Mitchell, K. E., Benjamin, S., Smirnova, T., Ritchie, H., Hogue, R., and Radeva, E., 1999. Assessment of land-surface energy budgets from regional and global models. *Journal of Geophysical Research*, **104**(D16), 19329–19348.

Burke, J. J., and Oliver, M. J., 1993. Optimal thermal environments for plant metabolic processes (*Cucumis sativus* L.) (light-harvesting chlorophyll a/b pigment-protein complex of photosystem II and seedling establishment in cucumber). *Plant Physiology*, **102**(1), 295–302.

Chao, H., Baumann, M., Jensen, A., Chen, Y., Cao, Y., Ren, W., and McKee, M., 2008. Band-reconfigurable multi-UAV-based cooperative remote sensing for real-time water management and distributed irrigation control. In *Proceedings of the 17th World Congress, International Federation*. Automatic Control, July 6–11, 2008, Seoul, pp. 11744–11749.

Cohen, Y., Alchanatis, V., Meron, M., Saranga, Y., and Tsipris, J., 2005. Estimation of leaf water potential by thermal imagery and spatial analysis. *Journal of Experimental Botany*, **56**(417), 1843–1852.

Colaizzi, P. D., Barnes, E. M., Clarke, T. R., Choi, C. Y., Waller, P. M., Haberland, J., and Kostrzewski, M., 2003. Water stress detection under high frequency sprinkler irrigation with water deficit index. *Journal of Irrigation and Drainage Engineering*, **129**(1), 36–43.

Colaizzi, P. D., Evett, S. R., Howell, T. A., and Tolk, J. A., 2006. Comparison of five models to scale daily evapotranspiration from one time of day measurements. *Transactions of the ASABE*, **49**(5), 1409–1417.

Colaizzi, P. D., Bliesner, R. D., and Hardy, L. A., 2008. A review of evolving critical priorities for irrigated agriculture. In *Proceeding of the World Environmental and Water Resources Congress 2008 Ahupua'a*. May 12–16, 2008, Honolulu: American Society of Civil Engineers, Environmental and Water Resources Institute.

Colaizzi, P. D., Evett, S. R., Howell, T. A., Gowda, P. H., O'Shaughnessy, S. A., Tolk, J. A., Kustas, W. P., and Anderson, M. C., 2012. Two source energy balance model-refinements and lysimeter tests in the Southern High Plains. *Transactions of the ASABE*, **55**(2), 551–562.

Crow, W. T., Kustas, W. P., and Prueger, J., 2008. Monitoring root-zone soil moisture through the assimilation of a thermal remote sensing-based soil moisture proxy into a water balance model. *Remote Sensing of Environment*, **112**, 1268–1281.

Evans, R. G., and Sadler, E. J., 2008. Methods and technologies to improve efficiency of water use. *Water Resources Research*, **44**, W00e04, doi: 10.1029/2007WR006200.

Evett, S. R., 2007. Soil water and monitoring technology. In Lascano, R. J., and Sojka, R. E. (eds.), *Irrigation of Agricultural Crops*, 2nd edn. Madison, WI: American Society of Agronomy/ Crop Science Society of America/Soil Science Society of America. Agronomy Monogr, Vol. 30, pp. 25–84.

Evett, S. R., and Alchanatis, V. L., 2007. *Improved analysis of thermally sensed crop water status and mapping spatial variability for site specific irrigation scheduling*. Final Report to BARD and the Texas Department of Agriculture on project TIE04-01. USDA-ARS Conservation and Production Research Laboratory, Bushland.

Evett, S. R., and Lascano, R. J., 1993. ENWATBAL.BAS: a mechanistic evapotranspiration model written in compiled BASIC. *Agronomy Journal*, **85**(3), 763–772.

Evett, S. R., Howell, T. A., Schneider, A. D., Upchurch, D. R., and Wanjura, D. F., 1996. Canopy temperature based automatic irrigation control. In Camp, C. R., et al. (eds.), In *Proceedings of the International Conference Evapotranspiration and Irrigation Scheduling*, San Antonio, ASAE, St. Joseph, November 3–6, 1996, pp. 207–213.

Evett, S. R., Howell, T. A., Schneider, A. D., Upchurch, D. R., and Wanjura, D. F., 2000. Automatic drip irrigation of corn and soybean. In Evans, R. G., Benham, B. L., and Trooien, T. P. (eds.), In *Proceedings of the 4th Decennial National Irrigation Symposium*. Phoenix, November 14–16, pp. 401–408.

Evett, S. R., Peters, R. T., and Howell, T. A., 2006a. Controlling water use efficiency with irrigation automation: cases from drip and center pivot irrigation of corn and soybean. In *Proceedings of the 28th Annual Southern Conservation Systems Conference*, Amarillo, June 26–28, 2006, pp. 57–66.

Evett, S. R., Tolk, J. A., and Howell, T. A., 2006b. Soil profile water content determination: sensor accuracy, axial response, calibration, temperature dependence and precision. *Vadose Zone Journal*, **5**, 894–907.

Evett, S. R., Heng, L. K., Moutonnet, P., and Nguyen, M. L., (eds.). 2008. *Field Estimation of Soil Water Content: A Practical Guide to Methods, Instrumentation, and Sensor Technology.* IAEA-TCS-30. Vienna: International Atomic Energy Agency, ISSN 1018–5518.

Evett, S. R., Tolk, J. A., and Howell, T. A., 2009. Soil profile water content determination in the field: spatio-temporal variability of electromagnetic and neutron probe sensors in access tubes. *Vadose Zone Journal*, **8**, 926.

Evett, S. R., Schwartz, R. C., Howell, T. A., Baumhardt, R. L., and Copeland, K. S., 2012a. Can weighing lysimeter ET represent surrounding field ET well enough to test flux station measurements of daily and sub-daily ET? *Advances in Water Resources*, **50**, 79–90.

Evett, S. R., Kustas, W. P., Gowda, P. H., Prueger, J. H., and Howell, T. A., 2012b. Overview of the Bushland Evapotranspiration and Agricultural Remote sensing EXperiment 2008 (BEAREX08): a field experiment evaluating methods quantifying ET at multiple scales. *Advances in Water Resources*, **50**, 4–19.

French, A. N., Hunsaker, D. J., Clarke, T. R., Fitzgerald, G. J., Luckett, W. E., and Pinter, P. J., Jr., 2007. Energy balance estimation of evapotranspiration for wheat grown under variable management practices in Central Arizona. *Transactions of the ASABE*, **50**(6), 2059–2071.

Gowda, P. H., Chavez, J. L., Colaizzi, P. D., Evett, S. R., Howell, T. A., and Tolk, J. A., 2007. Remote sensing based energy balance algorithms for mapping ET: current status and future challenges. *Transactions of the ASABE*, **50**(5), 1639–1644.

Gowda, P. H., Chavez, J. L., Colaizzi, P. D., Evett, S. R., Howell, T. A., and Tolk, J. A., 2008. ET mapping for agricultural water management: present status and challenges. *Irrigation Science*, **26**(3), 223–237.

Ha, W., Gowda, P. H., and Howell, T. A., 2013a. A review of downscaling methods for remote sensing-based irrigation management: part I. *Irrigation Science*, **31**, 831–850.

Ha, W., Gowda, P. H., and Howell, T. A., 2013b. A review of potential image fusion methods for remote sensing-based irrigation management: part II. *Irrigation Science*, **31**, 851–869.

Hatfield, J. L., Quisenberry, J. E., and Dilbeck, R. E., 1987. Use of canopy temperatures to identify water conservation in cotton germplasm. *Crop Science*, **27**, 269–273.

Heilman, J. L., Heilman, W. E., and Moore, D. G., 1982. Evaluating the crop coefficient using spectral reflectance. *Agronomy Journal*, **74**(6), 967–971.

Herwitz, S. R., Johnson, L. F., Dunagan, S. E., Higgins, R. G., Sullivan, D. V., Zheng, J., Lobitz, B. M., Leung, L. G., Gallmeyer, B., Aoyagi, M., Slye, R. E., and Brass, J., 2004. Imaging from an unmanned aerial vehicle: agricultural surveillance and decision support. *Computers and Electronics in Agriculture*, **44**, 49–61.

Howell, T. A., Meek, D. W., Phene, C. J., Davis, K. R., and McCormick, R. L., 1984. Automated weather data collection for research on irrigation scheduling. *Transactions of ASAE*, **27**(2), 386–391. 396.

Howell, T. A., Schneider, A. D., Dusek, D. A., Marek, T. A., and Steiner, J. L., 1995. Calibration and scale performance of Bushland weighing lysimeters. *Transactions of the ASABE*, **38**(4), 1019–1024.

Hunsaker, D. J., Barnes, E. M., Clarke, T. R., Fitzgerald, G. J., and Pinter, P. J., Jr., 2005. Cotton irrigation scheduling using remotely sensed and FAO-56 basal crop coefficients. *Transactions of ASAE*, **48**(4), 1395–1407.

Hunsaker, D. J., Fitzgerald, G. J., French, A. N., Clarke, T. R., Ottman, M. J., and Pinter, P. J., Jr., 2007. Wheat irrigation management using multispectral crop coefficients: I crop evapotranspiration prediction. *Transactions of the ASABE*, **50**(6), 2017–2033.

Idso, S. B., Jackson, R. D., and Reginato, R. J., 1977. Remote sensing of crop yields. *Science*, **196**, 19–25.

Idso, S. B., Jackson, R. D., Pinter, P. J., Reginato, R. J., and Hatfield, J. L., 1981. Normalizing the stress degree day for environmental variability. *Agricultural Meteorology*, **24**, 45–55.

Jackson, R. D., 1984. Remote sensing of vegetation characteristics for farm management. *Proceedings of SPIE*, **475**, 81–96.

Jackson, T. J., and Hsu, A. Y., 2001. Soil moisture and TRMM microwave imager relationships in the Southern Great Plains 1999 (SGP99) experiment. *IEEE Transactions on Geoscience and Remote Sensing*, **39**, 1632–1642.

Jackson, R. D., Idso, S. B., Reginato, R. J., and Pinter, P. J., Jr., 1981. Canopy temperatures as a crop water stress indicator. *Water Resources Research*, **17**(4), 1133–1138.

Jackson, R. D., Kustas, W. P., and Choudhury, B. J., 1988. A reexamination of the crop water stress index. *Irrigation Science*, **9**, 309–317.

Jackson, T. J., Le Vine, D. M., Swift, C. T., Schmugge, T. J., and Schiebe, F. R., 1995. Large area mapping of soil moisture using the ESTAR passive microwave radiometer in Washita'92. *Remote Sensing of Environment*, **53**, 27–37.

Jackson, T. J., Le Vine, D. M., Hsu, A. Y., Oldak, A., Starks, P. J., Swift, C. T., Isham, J. D., and Haken, M., 1999. Soil moisture mapping at regional scales using microwave radiometry: the Southern Great Plains hydrology experiment. *IEEE Transactions on Geoscience and Remote Sensing*, **37**(5), 2136–2151.

Jackson, T. J., Bindlish, R., Gasiewski, A. J., Stankov, B., Klein, M., Njoku, E. G., Bosch, D., Coleman, T. L., Laymon, C., and Starks, P., 2005. Polarimetric scanning radiometer C and X band microwave observations during SMEX03. *IEEE Transactions on Geoscience and Remote Sensing*, **43**, 2418–2430.

Jackson, T. J., Moran, M. S., and O'Neill, P. E., 2008. Introduction to soil moisture experiments 2004 (SMEX04). *Remote Sensing of Environment*, **112**, 301–303.

Jensen, M. E., 1968. Water consumption by agricultural plants. In Kozlowski, T. T. (ed.), *Water Deficits and Plant Growth*. New York: Academic, Vol. II, pp. 1–22.

Jensen, M. E., Burman, R. D., and Allen, R. G. (eds.), 1990. *Evaporation and irrigation water requirements*. New York: American Society of Civil Engineers. ASCE Manuals and Reports on Eng. Practices No. 70, p. 360.

Johnson, L., and Scholasch, T., 2005. Remote sensing of shaded areas in vineyards. *HortTechnology*, **15**(4), 859–863.

Jones, H. G., 1992. *Plants and Microclimate*, 2nd edn. Cambridge, UK: Cambridge Press.

Kim, Y., Evans, R. G., and Iversen, W. M., 2008. Remote sensing and control of an irrigation system using a wireless sensor network. *IEEE Transactions on Instrumentation and Measurement*, **57**(7), 1379–1387.

Kim, Y., Evans, R. G., and Iversen, W. M., 2009. Evaluation of closed-loop site-specific irrigation with wireless sensor network. *Journal of Irrigation and Drainage Engineering*, **135**(1), 25–31.

Kimball, B. A., LaMorte, R. L., Pinter, P. J., Jr., Wall, G. W., Hunsaker, D. J., Adamsen, F. J., Leavitt, S. W., Thompson, T. L., Matthias, A. D., and Brooks, T. J., 1999. Free-air CO_2 enrichment and soil nitrogen effects on energy balance and evapotranspiration of wheat. *Water Resources Research*, **35**, 1179–1190.

King, B. A., Wall, R. W., and Wall, L. R., 2000. *Supervisory Control and Data Acquisition System for Closed-Loop Center Pivot Irrigation*. ASABE Paper No. 002020. St. Joseph: ASABE.

Kustas, W. P., and Norman, J. M., 1999. Evaluation of soil and vegetation heat flux predictions using a simple two-source model with radiometric temperatures for partial canopy cover. *Agricultural and Forest Meteorology*, **94**, 13–29.

Kustas, W. P., Norman, J. M., Schmugge, T. J., and Anderson, M. C., 2004. Mapping surface energy fluxes with radiometric temperature. In Quattrochi, D., and Luvall, J. (eds.), *Thermal Remote Sensing in Land Surface Processes*. Boca Raton: CRC Press, pp. 205–253.

Kustas, W. P., Agam, N., Anderson, M. C., Li, F., and Colaizzi, P. D., 2007. Potential errors in the application of thermal-based energy balance models with coarse resolution data. In Neale, C. M. U., Owe, M., and D'Urso, G. (eds.), *Remote Sensing for Agriculture, Ecosystems, and Hydrology IX*. Proc. of SPIE, Vol. 6742, doi: 10.1117/12.737776. 674208, (2007) 0277-786X/07/$18.

Mazahrih, N. T., Katbeh-Bader, N., Evett, S. R., Ayars, J. E., and Trout, T. J., 2008. Field calibration accuracy and utility of four down-hole water content sensors. *Vadose Zone Journal*, **7**, 992–1000.

Miranda, F. R., Yoder, R., and Wilkerson, J. B. 2003. *A Site-Specific Irrigation Control System*. ASABE Paper No. 031129. St. Joseph: American Society of Agricultural and Biological Engineers.

Möller, M., Alchanatis, V., Cohen, Y., Meron, M., Tsipris, J., Naor, A., Ostrovsky, V., Sprintsin, M., and Cohen, S., 2007. Use of thermal and visible imagery for estimating crop water status of irrigated grapevine. *Journal of Experimental Botany*, **58**(4), 827–838.

Monteith, J. L., 1965. Evaporation and environment. In Fogg, G. E. (ed.), *Symposium of the Society for Experimental Biology, The State and Movement of Water in Living Organisms*. New York: Academic, Vol. 19, pp. 205–234.

Moran, M. S., 1994. Irrigation management in Arizona using satellites and airplanes. *Irrigation Science*, **15**, 35–44.

Moran, M. S., Clarke, T. R., Inoue, Y., and Vidal, A., 1994. Estimating crop water deficit using the relation between surface-air temperature and spectral vegetation index. *Remote Sensing of Environment*, **49**, 246–263.

Moran, M. S., Mass, S. J., and Pinter, P. J., Jr., 1995. Combining remote sensing and modeling for estimating surface evaporation and biomass production. *Remote Sensing Reviews*, **12**(4), 335–353.

Moran, M. S., Inoue, Y., and Barnes, E. M., 1997. Opportunities and limitations for image-based remote sensing in precision crop management. *Remote Sensing of Environment*, **61**, 319–346.

Neale, C. M. U., Jayanthi, H., and Wright, J. L., 2003. Crop and irrigation water management using high-resolution airborne remote sensing. In *Proceedings of ICID Workshop Remote Sensing of ET for Large Regions, CD-ROM*. New Delhi: International Commission on Irrigation and Drainage.

Norman, J. M., Kustas, W. P., and Humes, K. S., 1995. A two-source approach for estimating soil and vegetation energy fluxes from observations of directional radiometric surface temperature. *Agricultural and Forest Meteorology*, **77**, 263–293.

Norman, J. M., Anderson, M. C., Kustas, W. P., French, A. N., Mecikalski, J., Torn, R., Diak, G. R., Schmugge, T. J., and Tanner, B. C. W., 2003. Remote sensing of surface energy fluxes at 101-m pixel resolutions. *Water Resources Research*, **39**(8), 1221.

O'Shaughnessy, S. A. and Evett, S. R., 2007. IRT wireless interface for automatic irrigation scheduling of a center pivot system. In *Conference Proceedings of the 28th Annual International Irrigation Show*, San Diego Convention Center, San Diego, December 9–11, 2007. Reston: Irrigation Association, pp. 176–186.

O'Shaughnessy, S. A., and Evett, S. R., 2008. Integration of wireless sensor networks into moving irrigation systems for automatic irrigation scheduling. In *2008 ASABE Annual International Meeting*, Rhode Island Convention Center, Providence, Rhode Island, June 29–July 2, 2008. American Society of Agricultural and Biological Engineers. Paper No. 083452.

O'Shaughnessy, S. A., Evett, S. R., Colaizzi, P. D., and Howell, T. A., 2008. Soil water measurement and thermal indices for center pivot irrigation scheduling. In *Proceedings of the 2008 Irrigation Show and Conference*, November 2–4, 2008. Anaheim: Irrigation Association, Reston.

Penman, H. L., 1948. Natural evaporation from open water, bare soil, and grass. *Proceedings of the Royal Society of London*, **A193**, 120–146.

Peters, R. T., and Evett, S. R., 2004. Modeling diurnal canopy temperature dynamics using one time-of-day measurements and a reference temperature curve. *Agronomy Journal*, **96**, 1553–1561.

Peters, R. T., and Evett, S. R., 2007. Spatial and temporal analysis of crop stress using multiple canopy temperature maps created with an array of center-pivot-mounted infrared thermometers. *Transactions of the ASABE*, **50**(3), 919–927.

Peters, R. T., and Evett, S. R., 2008. Automation of a center pivot using the temperature-time-threshold method of irrigation scheduling. *Journal of Irrigation and Drainage Engineering*, **134**(3), 286–291.

Phene, C. J., Howell, T. A., and Sikorski, M. D., 1985. A traveling trickle irrigation system. In Hillel, D. (ed.), *Advances in Irrigation*. Orlando, FL: Academic, Vol. 3, pp. 1–49.

Plant, R. E., Munk, D. S., Roberts, B. R., Vargas, R. L., Rains, D. W., Travis, R. L., and Hutmacher, R. B., 2000. Relationships between remotely sensed reflectance data and cotton growth and yield. *Transactions of ASAE*, **43**(3), 535–546.

Postel, S., 1999. *Pillar of Sand, Can the Irrigation Miracle Last? Worldwatch Institute*. New York: W.W. Norton, p. 312.

Sadler, E. J., Bauer, P. J., Busscher, W. J., and Millen, J. A., 2000. Site-specific analysis of a droughted corn crop: II Water use and stress. *Agronomy Journal*, **92**(3), 403–410.

Sadler, E. J., Camp, C. R., and Evans, R. G., 2007. New and future technology. In Lascano, R. J., and Sojka, R. E. (eds.), *Irrigation of Agricultural Crops*, 2nd edn. Madison: American Society of Agronomy/Crop Science Society of America/Soil Science Society of America. Agronomy Monograph, Vol. 30, pp. 609–626.

Sela, E., Cohen, Y., Alchanatis, V., Saranga, Y., Cohen, S., Möller, M., Meron, M., Bosak, A., Tsipris, J., and Orolov, V., 2006. Use of thermal imaging for estimating and mapping crop water stress in cotton. In *6th European Conference on Precision Agriculture*, 3–6 June 2006, Skiathos.

Shock, C. C., David, R. J, Shock, C. A., and Kimberling, C. A. (1999) Innovative, automatic, low-cost reading of Watermark soil moisture sensors. In *Proceedings of the 1999 Irrigation Association Technical Conference*. Falls Church: Irrigation Association, pp. 147–152.

Todd, R. W., Evett, S. R., and Howell, T. A., 2000. The Bowen ratio-energy balance method for estimating latent heat flux of irrigated alfalfa evaluated in a semi-arid, advective environment. *Agricultural and Forest Meteorology*, **103**, 335–348.

Twine, T. E., Kustas, W. P., Norman, J. M., Cook, D. R., Houser, P. R., Meyers, T. P., Prueger, J. H., Starks, P. J., and Wesley, M. L., 2000. Correcting eddy-covariance flux underestimates over a grassland. *Agricultural and Forest Meteorology*, **103**, 279–300.

Upchurch, D. R., Wanjura, D. F., Burke, J. J., and Mahan, J. R., 1996. Biologically-identified optimal temperature interactive console (BIOTIC) for managing irrigation. United States Patent 5,539,637, July 23, 1996.

Verhoest, N. E. C., Lievens, H., Wagner, W., Álvarez-Mozos, J., Moran, M. S., and Mattia, F., 2008. On the soil roughness parameterization problem in soil moisture retrieval of bare surfaces from synthetic aperture radar. *Sensors*, **8**, 4213–4248.

Wall, R. W., and King, B. A., 2004. Incorporating plug and play technology into measurement and control systems for irrigation management. ASABE Paper No. 042189. St. Joseph: American Society of Agricultural and Biological Engineers.

Xiang, H., and Tian, L., 2007. Autonomous aerial image georeferencing for an UAV-Based data collection platform using integrated navigation system. Paper Number: 073046. St. Joseph: American Society of Agricultural and Biological Engineers.

Zhan, X., Crow, W. T., Jackson, T. J., and O'Neill, P., 2008. Improving space-borne radiometer soil moisture retrievals with alternative aggregation rules for ancillary parameters in highly heterogeneous vegetated areas. *IEEE Transaction on Geoscience and Remote Sensing*, **2**, 261–265.

Cross-references

Calibration, Optical/Infrared Passive Sensors
Commercial Remote Sensing
Crop Stress
Emerging Technologies, Sensor Web
Microwave Radiometers
Observational Platforms, Aircraft, and UAVs
Observational Systems, Satellite
Optical/Infrared, Radiative Transfer
Precision Agriculture
Rainfall
Remote Sensing, Physics and Techniques
Soil Moisture
Soil Properties
Surface Radiative Fluxes
Surface Water
Thermal Radiation Sensors (Emitted)
Vegetation Indices
Water and Energy Cycles
Water Resources